minerals

MDPI

Article

The Use of Hydrogen as a Potential Reductant in the Chromite Smelting Industry

Jamey Davies [1], Dogan Paktunc [2], José Juan Ramos-Hernandez [3], Merete Tangstad [4], Eli Ringdalen [5], Johan P. Beukes [1], Dmitri G. Bessarabov [6] and Stephanus P. Du Preez [6,*]

1 Chemical Resource Beneficiation (CRB), Faculty of Natural and Agricultural Sciences, Potchefstroom Campus, North-West University, Private Bag X6001, Potchefstroom 2520, South Africa; daviesjamey@gmail.com (J.D.); paul.beukes@nwu.ac.za (J.P.B.)
2 Canmetmining, Natural Resources Canada, 555 Booth St., Ottawa, ON K1A 0G1, Canada; dogan.paktunc@nrcan-rncan.gc.ca
3 Instituto de Ciencias Físicas, Universidad Nacional Autónoma de México, Cuernavaca 62210, Morelos, Mexico; jjramos@icf.unam.mx
4 Department of Material Science and Engineering, Norwegian University of Science and Technology (NTNU), Alfred Getz vei 2, 7034 Trondheim, Norway; merete.tangstad@ntnu.no
5 Sintef Industry, 7465 Trondheim, Norway; eli.ringdalen@sintef.no
6 Hydrogen South Africa (HySA) Infrastructure, Faculty of Engineering, Potchefstroom Campus, North-West University, Private Bag X6001, Potchefstroom 2520, South Africa; dmitri.bessarabov@nwu.ac.za
* Correspondence: faan.dupreez@nwu.ac.za

Abstract: The chromium (Cr) content of stainless steel originates from recycled scrap and/or ferrochrome (FeCr), which is mainly produced by the carbothermic reduction of chromite ore. Ever-increasing pressure on FeCr producers to curtail carbon emissions justifies migration from traditional FeCr production routes. The interaction between hydrogen and chromite only yields water, foregoing the generation of significant volumes of CO-rich off-gas during traditional smelting procedures. For this reason, the use of hydrogen as a chromite reductant is proposed. In addition to thermodynamic modelling, the influence of temperature, time, and particle size on the reduction of chromite by hydrogen was investigated. It was determined that, at the explored reduction parameters, the iron (Fe)-oxides presented in chromite could be metalized and subsequently removed by hot-acid leaching. The Cr-oxide constituency of chromite did not undergo appreciable metalization. However, the removal of Fe from the chromite spinel allowed the formation of eskolaite with the composition of $(Cr_{1.4}Al_{0.6})O_3$ in the form of an exsolved phase, which may adversely affect the reducibility of chromite. The study includes the limitations of incorporating hydrogen as a reductant into existing FeCr production infrastructure and proposes possible approaches and considerations.

Keywords: chromite; hydrogen; ferrochrome/ferrochromium; pre-reduction

Citation: Davies, J.; Paktunc, D.; Ramos-Hernandez, J.J.; Tangstad, M.; Ringdalen, E.; Beukes, J.P.; Bessarabov, D.G.; Du Preez, S.P. The Use of Hydrogen as a Potential Reductant in the Chromite Smelting Industry. *Minerals* **2022**, *12*, 534. https://doi.org/10.3390/min12050534

Academic Editor: Hongyu Zhao

Received: 24 March 2022
Accepted: 14 April 2022
Published: 25 April 2022

1. Introduction

Chromite ore is characterized by the unit formula $(Mg, Fe^{2+})(Al, Cr, Fe^{3+})_2O_4$ and serves as the only economically viable source of virgin Cr units [1,2]. The energy-intensive carbothermic smelting of chromite ore yields ferrochrome (FeCr)—a crude alloy of Cr and Fe [3–5]. Approximately 80 to 90% of produced FeCr is consumed by the stainless steel industry and is, therefore, considered equally important [4,6,7]. The significance of FeCr production is highlighted by the Cr constituency thereof, as the inclusion of Cr in stainless steel is the reason for the corrosion resistance thereof under standard ambient conditions [4].

Chromite smelting is typically performed in semi-closed or closed submerged arc furnaces (SAFs) and, to a lesser extent, closed direct current (DC) arc furnaces [6,8,9]. The energy consumption of a specific furnace is affected by factors such as material screening, chromite pre-heating, and pre-reduction [6]. For instance, the energy consumption of a

semi-closed SAF operating on unscreened feed materials can be as high as 4500 kWh/t FeCr produced, whereas a closed SAF operating on hot-fed pre-reduced chromite can be as low as 2000 kWh/t FeCr produced [6]. In addition to this, produced FeCr contains a certain amount of Si, which originates from the unintended reduction of silica in the slag phase, which increases energy consumption [10,11].

During chromite smelting, various types of carbon sources are used as reductants, e.g., coke, coal, and charcoal. The Cr- and Fe-oxide constituencies of chromite are reduced to their metallic states or carbide form [3,12]. For all these reduction reactions, CO(g) is formed and present in significant quantities in the off-gas. Due to the highly toxic nature of CO, the CO-rich off-gas must be oxidized before its release into the atmosphere. For semi-closed SAFs, this oxidation occurs above the furnace bed concurrently with smelting operations, while closed SAFs and DC furnaces oxidize CO-rich off-gas on a furnace stack [13–15].

Due to the nature of semi-closed SAFs, relatively significant quantities of air enter the space above the furnace bed and off-gas duct, and these SAFs produce between 10,000 to 15,000 Nm^3/t FeCr off-gas. Closed SAFs generate the lowest volumes of off-gas during smelting (i.e., 650 to 850 Nm^3/t FeCr), which are cleaned in venturi scrubbers before being flared or employed as fuel elsewhere on-site. The volume and CO-content of off-gas during closed SAF operations are, however, dependent on the leakage air [13,16]. Nevertheless, significant quantities of CO_2 are produced during chromite smelting, regardless of the furnace type and smelting regime employed.

Increasing pressure on the FeCr industry to curb C-emissions calls for the development of alternative smelting processes. Such processes should achieve high levels (preferably near-complete) of chromite reduction, while reducing C-emissions (when compared with traditional smelting processes). A recent patent by Winters (2016) proposed a process to produce Cr-containing alloy without employing SAFs [17]. This process utilizes a vertical moving reactor bed with external burners that consume pre-heated reformed natural gas (CO and hydrogen) to supply heat to the reactor, while concurrently injecting reformed natural gas into the bottom of the reactor. By doing so, the chromite is reduced in a solid state. Thereafter, the Cr-containing alloy is recovered through physical separation based on differences in density and magnetic properties of the alloy. This smelting process consumes approximately a third of the electrical energy required during conventional chromite smelting. Water and CO_2 are generated during this smelting process, of which the CO_2 is captured, compressed, and supplied to various industries. Significant quantities of naturally occurring natural gas are, however, a pre-requisite for this smelting method [17].

A patent by Pheiffer and Cookson (2015) suggested that SiC can be employed as a reductant during the FeCr production process. SiC composites can be incorporated during the generation of chromite agglomerates (e.g., briquettes or pellets) destined for oxidative sintering or pre-reductive pellet curing. The proposed SiC composite comprises mainly SiC, C, and ash (various fractions of CaO, MgO, SiO_2, Al_2O_3, FeO). The reaction of SiC with chromite yielded SiO_2 and CO as by-products; SiO_2 suggests that CO formation was partially reduced [18]. However, Pheiffer and Cookson (2015) did not perform a techno-economical study, and due to the cost of SiC, the running operational cost of a furnace operating on SiC-based reductants will likely be higher than traditional smelting operations [5].

A solid-state chromite reduction process was investigated by Yu and Paktunc (2018) where segregation reduction was implemented. During the process, graphite, petroleum coke, and charcoal were used as reductants, and calcium chloride ($CaCl_2$) as the segregation catalyst. This flux-assisted process achieved high degrees of Cr metalization at 1300 °C after 2 h of reduction in a rotary kiln or rotating hearth furnace. The $CaCl_2$ initiated the chlorination system that enabled the reducible Cr and Fe species from the chromite particles to segregate before the reduction and metalization by carbon. Subsequently, individual alloy particles were formed, which made the separation during ferrochrome recovery easier [19]. The $CaCl_2$ also provided a liquid media for the incongruent dissolution of chromite and migration of the reducible ions (e.g., Fe^{2+}, Fe^{3+}, Cr^{3+}). It was also possible to recover $CaCl_2$

in the reduced product through water-leaching; the catalyst could then be re-used and this would possibly save on material cost [20]. However, $CaCl_2$ could react with the siliceous gangue (e.g., clinochlore), causing the formation of Ca-bearing chromite, wadalite, and gaseous chlorides ($MgCl_2$, $FeCl_2$, and/or HCl). In the $CaCl_2$-assisted segregation reduction process, the ferrochrome alloy particles must be separated from the unwanted gangue present in the reduced products. Separation could likely succeed through conventional gravity or magnetic concentration techniques; however, further process development was proposed [19,21].

A patent by Sokhanvaran and Paktunc (2019) provided a method where the addition of cryolite (Na_3AlF_6) in chromite direct reduction was advantageous. The cryolite dissolved several oxides from the chromite spinel, which diminished slag growth. The forming molten cryolite layer enabled the migration of Cr and Fe ions. Impure mixtures containing cryolite (e.g., by-product of aluminum smelting processes and bath material produced as waste) were used in the chromite reduction. Using cryolite as an additive in chromite reduction involves several embodiments as well as many options of achieving these embodiments, enhancing the necessity for further research [22]. It is, however, noted that the use of F-containing reductants (as well as Cl-containing) are considered environmentally hazardous.

It has also been shown that the use of hydrocarbon gas for chromite reduction achieved higher degrees of reduction at lower temperatures when compared with traditional carbothermic smelting procedures [23].

To alleviate some C-dependence of chromite smelting, and to avoid the use of Cl- and F-containing compounds, the use of hydrogen as the reductant is proposed. Theoretically, the complete reduction of pure chromite by hydrogen is given as follows [24]:

$$Cr_2FeO_4 + 4\ H_2(g) = 2\ Cr + Fe + 4\ H_2O(g) \quad \text{(R1)}$$

It is noted that Reaction (1) requires temperatures greatly exceeding the typical temperatures associated with SAF smelting. In addition, the reduction of naturally occurring chromite does, however, proceed differently as the chromite spinel contains stabilizing Mg^{2+} and Al^{3+} [25]. Nevertheless, Reaction (1) shows that the only by-product when employing hydrogen as a reductant is water. Therefore, considering the occlusion of C-based by-products, the use of hydrogen to reduce chromite was explored in this study. More importantly, the reduction of Cr- and Fe-oxides was of importance, and the metalization mechanisms thereof were elucidated. It is proposed that by employing hydrogen to metalized chromite, or at least partially, the electrical and C consumption of a chromite smelter can be reduced.

2. Materials and Methods

2.1. Materials

Kleynhans et al. (2016) stated that in 2012 approximately 28% of globally smelted chromite originated from South Africa. Thus, a significant fraction of globally produced FeCr, which is estimated to be approximately 32%, originated from South African chromite [26,27]. Considering this, the results presented in this study are of international relevance.

Metallurgical-grade chromite ore was obtained from a large South African FeCr producer and was used as the case study ore. A homogeneous and representative sample collection campaign was undertaken at the South African FeCr smelter and sample selection for experimentation was applied here as described by Du Preez et al. (2019) [2]. A thorough characterization of this case study ore was conducted by Glastonbury et al. (2015) [28], therefore characterization was not repeated here. Table 1 summarizes the chemical and crystalline characteristics of chromite ore used here. Bulk chemical characteristics were determined by inductively coupled plasma–optical emission spectroscopy (ICP–OES) and bulk mineralogical composition by X-ray diffraction (XRD) analysis.

Table 1. Characterization of the case study chromite ore in terms of the chemical composition (ICP–OES, wt.%) [28], and mineralogical composition (XRD, wt.%).

ICP-OES		XRD	
Compound	**Metgrade**	**Compound**	**Metgrade**
Cr_2O_3	44.19	Chromite	93.4
FeO	24.68	Enstatite	6.6
SiO_2	2.96		
Al_2O_3	14.71		
MgO	10.31		
CaO	0.16		
P	0.001		
Cr/Fe	1.58		

Of particular importance here were the Cr- and Fe-contents, and the Cr/Fe ratio. It is worth noting that South African chromite has relatively low Cr-contents. For instance, Ringdalen and Olsen (1998) indicated that Turkish, Kazak, and Brazilian chromite ore contains 0.70–0.77 mol Cr in the octahedral sites, whereas South African ore contains between 0.59–0.62 mol Cr. As a result, octahedral sites are occupied by Al^{3+} and a relatively low amount of Fe^{3+} (around 0.06 mol) [29]. As stated earlier, the presence of Mg^{2+} (in tetrahedral sites) and Al^{3+} adversely affect the reducibility of chromite.

Hydrogen, which was the investigated reductant in this study, can be produced from numerous processes, e.g., thermochemical [30,31], photocatalytic [32,33], photochemical [34,35], photo-electrochemical [36,37], metal, and metal hydride hydrolysis [38–44], electrochemical [45–50], ammonia and formic acid decomposition [51–53], and various biological processes [54–56]. The hydrogen used throughout this study as the reductant was generated on-site at Hydrogen South Africa Infrastructure, South Africa, by proton exchange membrane water electrolysis (PEMWE). A PEMWE stack was powered by photovoltaic energy and the generated hydrogen was stored as a pressurized gas. Therefore, the hydrogen used here is defined as green hydrogen as it is produced from renewable energy and a renewable source. Nitrogen (99% purity) was obtained from Afrox, South Africa.

2.2. Sizing of Chromite

Size partitioning of as-received chromite ore was performed by screening it into the following size fractions, i.e., <106, 106 to 250, 250 to 500, and 500 to 1000 µm. Chromite screening was performed using a Haver EML Digital Plus sieve shaker and stainless- steel Haver and Boecker sieves.

Particle size distribution of the screened chromite fractions was performed by laser diffraction particle sizing using a Malvern Mastersizer 3000. Samples were ultra-sonicated before measurements and continuously agitated by mechanical stirring at 2400 rpm during analyses. Laser obscuration was maintained between 10 to 20%. The d_{90}, d_{50}, and d_{10} values of as-received and size fractioned are presented in Table 2.

Table 2. D_{90}, d_{50}, and d_{10} (µm) of as-received and size fractioned chromite.

Size Equivalent	As-Received	Sieve Sizes (µm)			
		<106	**106 to 250**	**250 to 500**	**500 to 1000**
d_{90}	415.0	140.2	282.1	464.2	924.1
d_{50}	182.3	87.4	186.3	347.4	667.7
d_{10}	71.7	51.8	120.7	260.0	487.6

2.3. Reduction Procedure

Reduction procedures were performed in a Carbolite vertical tube furnace; the furnace had a maximum operating and maintainable temperature of 1200 and 1100 °C, respectively. Ceramic heat shields were placed within the tube at both ends to increase the stability of

the heated zone. Stainless steel caps were fitted to seal the tube ends and acted as a gas inlet and outlet. The thermocouple used to measure temperature was located at the center of the heating zone, immediately adjacent to the tube. The furnace was heated by a series of electrodes which were located adjacent to the tube.

The reduction was performed by placing 50 g of chromite in a crucible in the center of the furnace hot zone. The samples were then heated from room temperature at the maximum allowable heating rate for the specifically fitted tube, i.e., 5 °C/min, until the predetermined temperature was reached. The tube was continuously purged with N_2 at a flow rate of 75 mL/min. It was of importance to ensure no oxygen was present within the furnace seeing that hydrogen has a self-ignition temperature of approximately 572–585 °C and an explosive range of 4–75 vol.% in air at standard ambient conditions [57–59]. A 1 L/min hydrogen flow, in conjuration with the N_2 flow, was introduced at 600 °C to obtain an approximate 93 vol.% hydrogen atmosphere within the furnace tube. This atmosphere was maintained until a pre-determined reduction temperature was reached/maintained. Thereafter, the hydrogen flow was discontinued, and the reduced samples were allowed to cool to room temperature in an N_2 atmosphere.

2.4. Analytical Techniques

Temperature programmed reduction (TPR) was performed using an automated chemisorption analyzer AutoChem II 2920 (Micrometrics, Norcross, GA, USA). Approximately 0.25 g of sample was placed in a quartz U-tube fitted with quartz wool which was fixed to the bottom of the tube. TPR analyses were performed using 10 vol.% H_2/Ar at a flow rate of 50 mL/min. Before analysis, the sample-containing tube was purged at room temperature for 30 min using the latter mentioned gas. Thereafter, the furnace was heated at a rate of 10 °C/min to 1000 °C while continuously recording hydrogen consumption with a thermal conductivity detector. This instrument had a maximum maintainable temperature of 1000 °C.

Scanning electron microscopy (SEM) equipped with an energy-dispersive x-ray spectrometer (EDX) was used to perform surface and subsurface characterization of unreduced/reduced chromite particles in backscattered electron mode. An FEI Quanta 250 FEG SEM incorporating an Oxford X-map EDX system operating at 15 kV and a working distance of 10 mm was used. For subsurface analysis, treated chromite particles were set in resin, cross-sectioned, and polished using an SS20 Spectrum System Grinder polisher before being mounted on Al stubs using carbon adhesive tape. All samples considered for SEM analysis were coated with carbon using an Emscope TB 500 carbon coater.

Crystalline phase analysis of bulk samples was performed by X-ray diffraction (XRD) utilizing a Rigaku D/MAX 2500 rotating-anode powder diffractometer with Cu Kα radiation at 50 kV, 260 mA, a step-scan of 0.02°, and a scan rate at 1/min in 2 h from 5 to 70°. Phase identification was performed using JADE v.3.9 with the ICDD and ICSD diffraction databases.

Further analysis was undertaken by mounting cross-sectioned polished pellets on glass slides and carbon-coating them before characterization by electron probe microanalysis (EPMA). EPMA analyses were performed to determine the oxidation states of the transformation products. Analysis was conducted using a JEOL JXA-8900 electron microprobe fitted with five wavelength dispersive spectrometers at an accelerating voltage of 20 kV and a beam current of 26 nA.

The extent of Cr and Fe metalization was determined after the reduction of chromite by solubilizing Cr and Fe through hot-acid leaching. The treated chromite was leached using a 50 vol.% H_2SO_4 solution at 90 °C for 60 min. Thereafter, the solubilized Cr and Fe contents were determined using ICP-OES.

ICP-OES was performed by using a 5110 ICP-OES Instrument coupled with a VistaChip II CCD detector. The instrument was calibrated using Ultraspec aqueous certified single-element reference standards (Fe, Cr) obtained from De Bruyn Spectroscopic Solutions (South Africa).

Considering that during size fractioning, gangue mineral (i.e., non-chromite, siliceous particles) particles could collect within a certain size range, the total Cr and Fe content of the respective size fraction were determined, and the extent of Cr and Fe metalization calculated as a function of the total Cr and Fe contents present in each size fraction.

A Siebtechnik pulverizer was used to mill each size fraction. All parts of the pulverizer that made contact with the chromite during milling were made of SiC to prevent Fe contamination during the milling procedure. A sample was milled for 2 min to obtain a particle-size distribution of which 90% of the particles were below 75 µm. Total Cr and Fe were determined for each size fraction by high-temperature alkaline fusion using Na_2O_2. Alkaline fusion was performed on all size fractions by reacting 0.2 g of the milled chromite with 2 g Na_2O_2 and 0.5 g Na_2CO_3, respectively, in a zirconium crucible. The fused material was then solubilized using a 20% mixture of 1:1 water:HNO_3 and the Cr and Fe contents were determined by ICP-OES.

2.5. Expressing the Extent of Metalization

Two terms are generally used to express the extent of Cr and Fe reduction; either in terms of lowering the oxidation state (e.g., Fe_2O_3 (Fe^{3+}) reduced to FeO (Fe^{2+})) or metalization (e.g., Cr_2O_3 reduced to Cr^0) [12]. Barnes et al. (1983) defined Reduction (%R) and Metalization (%M) as the follows:

The removal of oxygen is associated with %R and is defined in terms of the oxygen mass loss expressed in the equation below:

$$\%R = \frac{\text{Mass of oxygen removed}}{\text{Original removable oxygen}} \times 100 \quad (1)$$

in a case where solid carbon is used as a reductant, CO will form as a product in the reduction process of chromite and for this reason, the reduction can also be described as [12]:

$$\%R = \frac{\text{Mass of CO evolved}}{28/16 \text{ x original removable oxygen}} \times 100 \quad (2)$$

$$\%M = \frac{Cr^0 + Fe^0}{Cr_{tot} + Fe_{tot}} \times 100 \quad (3)$$

where Cr^0 and Fe^0 are the total amounts of metalized Cr and Fe, and Cr_{tot} and Fe_{tot} are the total Cr and Fe contents of the original chromite. Furthermore, Barnes et al. (1983) proposed that due to the possible concurrence of the reduction of Fe_2O_3 to FeO and metalization of FeO to Fe and Cr_2O_3 to Cr, there is no linear relationship between chromite's reduction and its metalization [12].

There is, however, a close resemblance between the complete removal of oxygen and complete metalization, as 100% reduction corresponds to 100% metalization [12]. The factors explained by Barnes et al. (1983) have contributed to the statement given by Algie and Finn (1984), which explains the three stages of chromite reduction: first, the Fe^{3+} is reduced to $Fe^{2+,}$ followed by its metalization; the metalization of Cr^{3+} is only initiated after approximately 50% of the Fe^{2+} is metalized. After the completion of Fe reduction, 60% of the Cr reduction could be achieved [60,61].

However, the reduction of chromite by C is relatively well understood and more descriptive expressions have been formulated. In this study, the %Fe and Cr metalization was of importance and expressed individually according to the following equation:

$$\%\text{Fe or Cr metalization} = \frac{\text{Solubilized Fe or Cr}}{\text{Total Fe or Cr content}} \times 100 \quad (4)$$

where the metalized Fe and Cr fractions of the treated chromite (defined as the fractions of leached Cr and Fe, as determined by ICP–OES analysis) are represented by the solubilized Fe or Cr value, which is divided by the total amount of Fe or Cr present in the untreated chromite ore. The metalization of Fe and Cr are presented individually.

3. Results and Discussion

3.1. Thermodynamic Considerations

When kinetic data are not available to characterize a process at elevated temperature, an alternative is to understand the thermochemical aspects that govern the behavior of the chemical species that are in reaction. Thermodynamic considerations are, however, required to understand what can be achieved, as well as the driving force for reduction to occur. The predominant area phase-stability diagrams are a tool that allows us to graphically represent the conditions of thermochemical equilibrium of compounds in reaction. The diagrams presented in this section were generated using the methodology proposed by Ramos-Hernandez et al. [62], using recently updated thermochemical data that were selected from various sources, both old and recent [63–67].

To graphically evaluate the thermochemical conditions of the Cr and Fe reduction processes from chromite (Cr_2FeO_4) using C or hydrogen as a reducing agent, it is necessary to identify the reduction regions of interest (where the Cr and Fe species predominate) for each of the processes in a (Cr, Fe)-C-H-O diagram, such as Figure 1, where the chemical activity of Cr and Fe are represented on the X and Y axes, respectively.

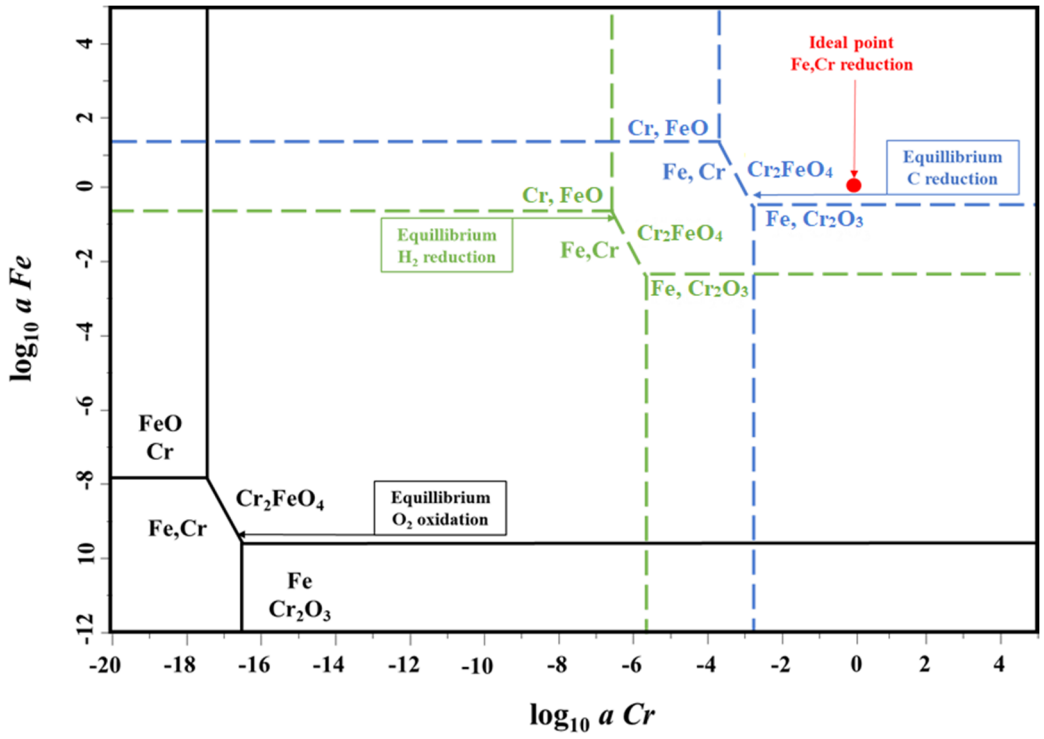

Figure 1. Phase stability diagrams of the (Cr, Fe)-C-H-O system as a function of partial pressure of H_2 and H_2O at a temperature of 1000 °C.

As references, the ideal point for the reduction of Cr and Fe is presented in red, considering that the chemical activity of each reduced metallic element takes the value of the unit (log aM = 1). Furthermore, the equilibrium lines in black correspond to the Cr_2FeO_4 reduction reactions in an environment containing O_2, where four regions of stability are defined where Cr_2FeO_4 predominates, and the following pairs of species: Fe-Cr, FeO-Cr, and Fe-Cr_2O_3 where the following decomposition reactions have been considered:

$$2\ FeO\ (s) \rightleftarrows 2\ Fe(s) + O_2 \quad \log K\ (1000\ ^\circ C) = 15.5563 \tag{R2}$$

$$2\ Cr_2FeO_4\ (s) \rightleftarrows 2\ Cr_2O_3(s) + 2\ Fe(s) + O_2 \quad \text{“} = 18.9956 \tag{R3}$$

$$Cr_2FeO_4\ (s) \rightleftarrows 2\ Cr(s) + Fe(s) + 2\ O_2 \quad \text{“} = 42.6068 \tag{R4}$$

$$Cr_2FeO_4\ (s) \rightleftarrows 2\ Cr(s) + Fe(s) + 2\ O_2 \quad \text{“} = 66.2180 \tag{R5}$$

$$2\ Cr_2FeO_4\ (s) \rightleftarrows 2\ FeO(s) + 4\ Cr(s) + 3\ O_2 \quad \text{“} = 69.6572 \tag{R6}$$

It is worth mentioning that there is a decomposition Reaction (7) that cannot be drawn on the diagram because it is independent of the variables being evaluated; however, its thermochemical viability can be evaluated as indicated below:

$$Cr_2FeO_4\ (s) \rightleftarrows 2\ Cr_2O_3(s) + 2\ FeO(s) \quad \log K\ (1000\ ^\circ C) = 14.4218 \tag{R7}$$

Each chemical reaction presents its corresponding value of the equilibrium constant (log K) at 1000 °C, which is related to the value of the standard Gibbs free energy as $\Delta G^\circ = -RT \log K$. Each set of reactions was written considering this value in descending order to carry out a numerical evaluation of the thermochemical conditions of each one of them since the thermochemical viability of a reaction can be evaluated numerically considering it inversely proportional to the absolute value of log K; however, when the log K value is zero, it is established that the reaction is in thermochemical equilibrium. Also, a positive value for log K indicates the thermochemical viability of the forward reaction (as written), while a negative value implies viability for the reverse reaction.

Based on the criteria described in the previous paragraph, all reduction reactions (Reactions (2)–(6)) are not viable, considering the negative value of log K and the magnitude of its absolute values; this is why these reactions were considered an extreme case of comparison. However, relatively, it can be identified that the reduction of Cr and Fe from Cr_2FeO_4 (Reaction (4)) is more viable than the reduction of Cr from Cr_2O_3 (Reaction (5)) by 23.6 orders of magnitude. Although Reactions (4) and (5) have lower viabilities than Reactions (2) and (3), the reduction of Fe from FeO (Reaction (2)) is relatively more viable than from Cr_2FeO_4 (Reaction (3)) by 3.5 orders of magnitude. Rection 6 is the reaction with the lowest thermochemical viability and its interpretation in the case study of this work is meaningless; however, it is imperative to define the area of stability for Cr_2FeO_4 on the phase stability diagram. Reaction (7) is practically more viable, even more so than Reaction (2); this is the reason why the reduction of Fe and Cr is typically evaluated from Reactions (2) and (4).

The equilibrium lines in blue correspond to reduction reactions using C as a reducing agent and considering only CO as a by-product (normally employed in carbothermic processes):

$$FeO(s) + C(s) \rightleftarrows Fe(s) + CO \quad \log K\ (1000\ ^\circ C) = 1.4196 \tag{R8}$$

$$Cr_2FeO_4\ (s) + C(s) \rightleftarrows Cr_2O_3(s) + Fe(s) + CO \quad \text{“} = 0.3000 \tag{R9}$$

$$Cr_2O_3(s) + 3\ C(s) \rightleftarrows 3\ CO + 2\ Cr(s) \quad \text{“} = 5.5156 \tag{R10}$$

$$Cr_2FeO_4\ (s) + 4\ C(s) \rightleftarrows 2\ Cr(s) + Fe(s) + 4\ CO \quad \text{“} = 5.8157 \tag{R11}$$

$$Cr_2FeO_4\ (s) + 3\ C(s) \rightleftarrows 2\ Cr(s) + FeO(s) + 3\ CO \quad \text{“} = 7.2353 \tag{R12}$$

It is well understood that during the carbothermic reduction of chromite, Fe-oxide reduction initiates before the Cr_2O_3 constituency [61,68]. Considering this, the reaction kinetics of pure Fe-oxides and Cr_2O_3 and with carbon and hydrogen was considered separately to gain insight into their expected reactivity. The carbothermic reduction of Fe- and Cr-oxides of chromite proceeds according to the following reactions (for naturally occurring chromite, both Fe^{3+} and Fe^{2+} are present) [12]:

In the first stages of reduction, Fe_2O_3 (Fe^{3+}) is reduced to FeO (Fe^{2+}) without any metalization,

$$Fe_2O_3 + C = 2\ FeO + CO \tag{R13}$$

Subsequently, metalization occurs as FeO (Fe^{2+}) is reduced to Fe^0 (Reaction (8)) and lastly, Cr_2O_3 (Cr^{3+}) is metalization to Cr^0 (Reaction (10)). Considering Reactions (3) and (4), the reduction and metalization of Fe-oxides should occur at 552 and 694 °C, respectively. Considering Reaction (10), the reduction of Cr_2O_3 proceeds at 1263 °C. It is worth noting

that during Reactions (8)–(13), hot CO gas is continuously generated which permeates from the smelting zone upwards through the furnace bed. The hot CO gas acts as a reductant, partially reducing chromite [69]. The effect of CO(g) partial pressure was, however, not considered here.

The reduction reactions of Fe- and Cr-oxides by hydrogen, in terms of oxidation state changes, will likely follow similar routes as Reactions (8)–(13). The equilibrium lines in green color correspond to reduction reactions and considers H_2O as a by-product:

$$FeO(s) + H_2 \rightleftarrows Fe(s) + H_2O \quad \log K\ (1000\ ^\circ C) = 0.5047 \tag{R14}$$

$$Cr_2FeO_4\ (s) + H_2 \rightleftarrows Cr_2O_3(s) + Fe(s) + H_2O \quad \text{“} = 2.2243 \tag{R15}$$

$$Cr_2O_3(s) + 3\ H_2 \rightleftarrows 2\ Cr(s) + 3\ H_2O \quad \text{“} = 11.2885 \tag{R16}$$

$$Cr_2FeO_4(s) + 3\ H_2 \rightleftarrows FeO(s) + 2\ Cr(s) + 3\ H_2O \quad \text{“} = 13.0081 \tag{R17}$$

$$Cr_2FeO_4(s) + 4\ H_2 \rightleftarrows Fe(s) + 2\ Cr(s) + 4\ H_2O \quad \text{“} = 13.5128 \tag{R18}$$

The presence of in-situ formed H_2O affects Reactions (14)–(18), and it has to be taken into account that these reactions proceed as a function of the partial pressure of both H_2 and H_2O [70,71].

In the diagram shown in Figure 1, the reduction region of the processes that use C and hydrogen as reductants tends to be closer to the ideal reduction point, than to the reduction region of the process in an environment rich in O_2; this indicates that the use of hydrogen as a reducing agent is a thermodynamically good alternative. Furthermore, the main advantage of using hydrogen as a reducing agent is that the main by-product of the process is H_2O, which means that it is a green alternative that contrasts with the greenhouse gases generated in the process that uses C as a reducing agent.

Figure 2 shows a full predominant area phase-stability diagram for the (Cr, Fe)-H_2-H_2O system, where the *Y*-axis represents the partial pressure of hydrogen, and the *X*-axis represents the partial pressure of H_2O. Considering the chemical activity of each of the condensed species of interest (which can be formed from the elements Cr, Fe, H, and O) as a unit, in such a way that the equilibrium lines that establish the stability region of each species correspond to the reduction Reactions (6) and (14) and another listed below:

$$2\ Fe(OH)_3\ (s) + H_2 \rightleftarrows 2\ Fe(OH)_2\ (s) + 2\ H_2O \quad \log K\ (1000\ ^\circ C) = 9.6678 \tag{R19}$$

$$2\ CrH\ (s) \rightleftarrows 2\ Cr\ (s) + H_2 \quad \text{“} = 7.8491 \tag{R20}$$

$$2\ CrH\ (s) + 4\ H_2O \rightleftarrows 2\ Cr(OH)_2\ (s) + 3\ H_2 \quad \text{“} = 5.9153 \tag{R21}$$

$$2\ Cr(OH)_3\ (s) + H_2 \rightleftarrows 2\ Cr(OH)_2\ (s) + 2\ H_2O \quad \text{“} = 5.9027 \tag{R22}$$

$$3\ Fe_2O_3\ (s) + H_2 \rightleftarrows 2\ Fe_3O_4\ (s) + H_2O \quad \text{“} = 4.8997 \tag{R23}$$

$$Fe(OH)_2\ (s) + H_2 \rightleftarrows Fe\ (s) + 2\ H_2O \quad \text{“} = 4.8199 \tag{R24}$$

$$Fe_3O_4\ (s) + H_2 \rightleftarrows 3\ FeO(s) + H_2O \quad \text{“} = 1.4717 \tag{R25}$$

$$FeO\ (s) + H_2O \rightleftarrows Fe(OH)_2\ (s) \quad \text{“} = -5.3245 \tag{R26}$$

$$Cr_2O_3\ (s) + H_2O + H_2 \rightleftarrows 2\ Cr(OH)_2\ (s) \quad \text{“} = -13.2223 \tag{R27}$$

$$Fe_3O_4\ (s) + 2\ H_2O + H_2 \rightleftarrows 3\ Fe(OH)_2\ (s) \quad \text{“} = -14.5019 \tag{R28}$$

$$Fe_2O_3\ (s) + 3\ H_2O \rightleftarrows 2\ Fe(OH)_3\ (s) \quad \text{“} = -17.7025 \tag{R29}$$

$$Cr_2O_3\ (s) + 3\ H_2O \rightleftarrows 2\ Cr(OH)_3\ (s) \quad \text{“} = -19.1249 \tag{R30}$$

$$Cr_2O_3\ (s) + 4\ H_2 \rightleftarrows 2\ CrH\ (s) + 3\ H_2O \quad \text{“} = -19.1376 \tag{R31}$$

$$2\ Fe_3O_4\ (s) + 10\ H_2O \rightleftarrows 6\ Fe(OH)_3\ (s) + H_2 \quad \text{“} = -58.0072 \tag{R32}$$

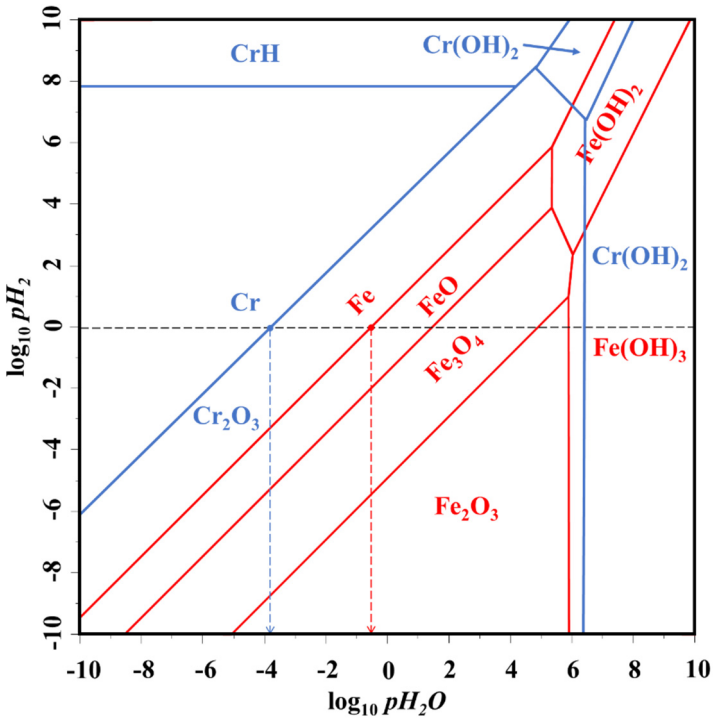

Figure 2. Phase stability diagrams of the (Fe, Cr)-H_2-H_2O system as a function of partial pressure of H_2 and H_2O at a temperature of 1000 °C.

The equilibrium lines in blue color correspond to the reactions involving Cr, while the equilibrium lines in red involve Fe. Also, the diagram shows a black dotted horizontal line that corresponds to the value of log pH_2 = 0 (that is, pH_2 = 1 atm), where two points are also located from the conditions of log pH_2O of equilibrium for the reduction reactions of Fe (reaction H, log $pH_2O \approx -0.5$) and Cr (reaction K, log $pH_2O \approx -4$). The above indicates that to exclusively reduce Fe and Cr in the system, there must be a partial pressure of H_2O less than or equal to 0.0001 atm; when this partial pressure is between 0.0001 and 0.3162 atm, the Fe and Cr_2O_3 species will predominate and if the partial pressure it is even greater, species such as Fe_3O_4, Fe_2O_3, $Fe(OH)_3$, $Cr(OH)_2$ will also predominate. Słowiński and Smoliński (2016) showed that the introduction of Fe to an H_2O-rich atmosphere will result in its oxidation to $Fe_{0.947}O$ (shown as FeO here) [70]. It can be seen from Figure 2 that Fe is stable in a relatively wide range of H_2/H_2O partial pressure ratios at 1000 °C, with decreasing stability as the partial pressure of H_2O increases. Cr is stable in a relatively small area, which corresponds to a high H_2/H_2O ratio (dry, H_2-rich atmosphere). Chu and Rahmel stated that the reduction of Cr_2O_3 is only possible in oxygen-free and dry hydrogen environments, if the in-situ generated H_2O is continuously removed from reaction sites [71].

Most of the reactions with a log K value greater than zero are found in the region where the partial pressure of hydrogen is greater than 1 atm, while the reduction reactions with a log K value less than zero are found in the region of partial pressure less than 1 atm, which corresponds to the experimental conditions of this study.

It is important to note that the oxides considered in this study form part of the chromite spinel, i.e., $[(Mg^{2+}, Fe^{2+})(Al^{3+}, Cr^{3+}, Fe^{3+})_2O_4]$ [1,72]. Chromite is considered isomorphic, with Mg^{2+} and/or Fe^{2+} occupying tetrahedral sites and Al^{3+}, Cr^{3+}, and/or Fe^{3+} occupying octahedral sites at standard ambient conditions [73]. The presence of Mg^{2+} and Al^{3+} greatly decreases the reducibility of the chromite because these cations form highly stable oxides. It is noted that a magnesium-containing chromite spinel, i.e., $(Fe^{2+}, Mg^{2+})Cr_2O_4$, has a greater resistance to reduction when compared with an Al-containing spinel, i.e., $Fe(Cr^{3+}, Al^{3+})_2O_4$ [23]. Nevertheless, although the reduction reactions (Reactions (2)–(32)) are for

pure Cr_2FeO_4, Fe- and Cr-oxides, the conclusions reached from the phase stability diagrams presented are consistent with the results of this work.

3.2. Reactivity of Chromite with Hydrogen

Though thermodynamic explanations of a reaction are a useful tool, they ignore kinetic effects. To determine the actual interaction between the case-study chromite and hydrogen, TPR analysis was performed on as-received chromite (Figure 3). The initiation of Fe-oxidation state reduction is included in Figure 3.

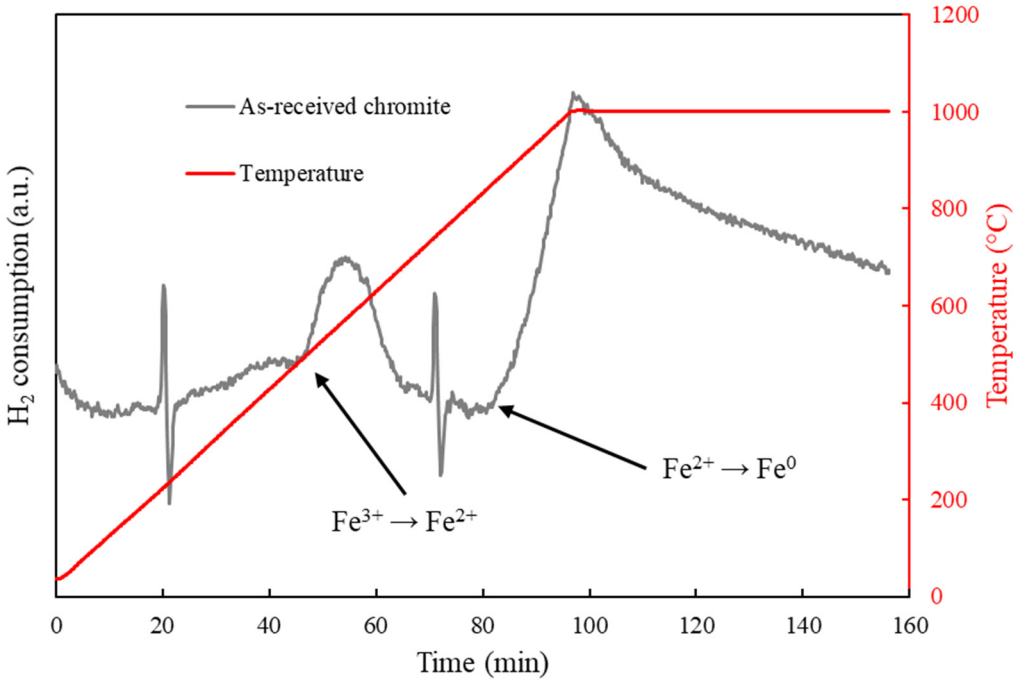

Figure 3. Temperature programmed reduction (TPR) profile of as-received chromite reduced in a 10 vol.% H_2/N_2 atmosphere at 1000 °C for 60 min.

Figure 3 presents the interaction between hydrogen and chromite as a function of temperature. When considering Figure 3, the following deductions may be made: (i) the reduction of Fe_2O_3 to FeO (Fe^{3+} to Fe^{2+}) initiated at approximately 500 °C; (ii) the peak observed at approximately 846 °C is likely the reduction of FeO to Fe (Fe^{2+} to Fe^0); (iii) no magnetite (expressible as $Fe(Fe^{3+})_2O_4$ or $FeOFe_2O_3$) to FeO reduction peak is observed, likely indicating that the intermediate step proceeds rapidly during the reduction of $Fe_2O_3 \rightarrow$ FeO; (iv) the reaction rate peaked after reaching 1000 °C and proceeded at a slower rate thereafter, suggesting hydrogen diffusion was likely limited by the formation of a surficial metallic layer and restricted hydrogen–chromite reaction surface, or that the reduction reaction rate decreased as a function of decreasing FeO concentration, or that mass transfer was limited due to a build-up of H_2O in the atmosphere surrounding the crucible; and (v) the absence of addition peaks suggests that Cr_2O_3 did not undergo observable reduction, which was expected considering thermodynamic calculations.

During thermal treatment of chromite, the constituents present in the chromite spinel migrate as a function of the atmosphere. For instance, Fe_2O_3-rich sesquioxide phases form at the rim of chromite particles, as well as the cleavage planes during calcination in air [2], whereas metalized Fe forms at the rims during carbon-based solid-state reduction [74]. To evaluate constituency mobility of chromite during reduction using hydrogen, the surface of as-received, reduced, and acid-leached chromite particles were explored by SEM (Figure 4) and EDX (Table 3). Reduced particles presented here were exposed to hydrogen at 1100 °C for 30 min. The acid-leached sample was imaged at a higher magnification than the as-received and treated samples to better illustrate the surface morphology.

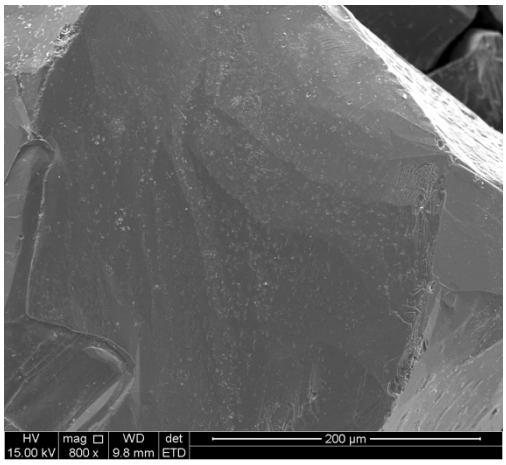

(**a**)

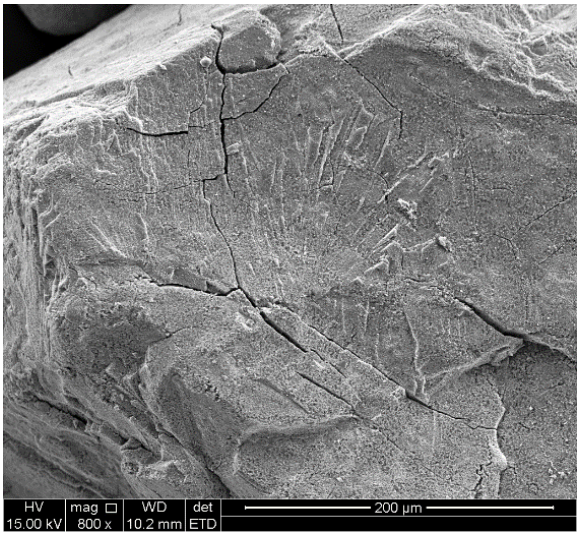

(**b**)

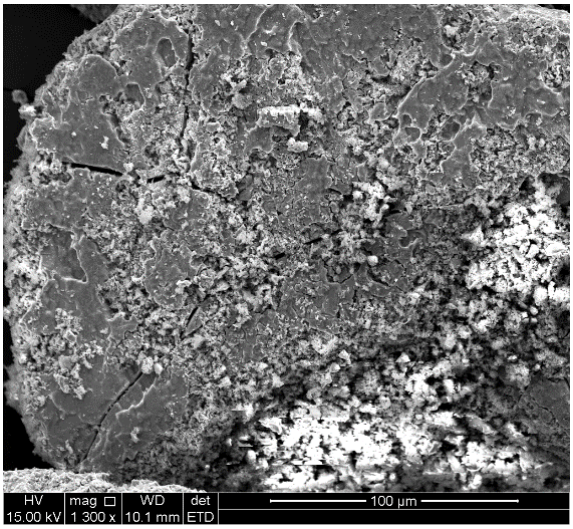

(**c**)

Figure 4. Backscattered electron SEM micrographs of the surface of as-received chromite (**a**), 800 times magnification), hydrogen-treated chromite (**b**), 800 times magnification), and acid-leached hydrogen-treated chromite (**c**), 1300 times magnification).

Table 3. Microanalyses of chromite particles by SEM–EDX (wt.%). A minimum of eight randomly selected particles were considered and between three to five areas were analyzed with the averages and standard deviations indicated. The Cr/Fe ratio is also indicated.

Sample Surface	Detected Element (wt.%)						Cr/Fe Ratio
	O	Mg	Al	Si	Cr	Fe	
As-received	36.68 ± 1.41	6.29 ± 0.30	8.45 ± 0.23	0.29 ± 0.01	30.85 ± 1.49	17.44 ± 0.52	1.77
Treated	26.32 ± 3.69	2.12 ± 0.49	13.69 ± 0.48	0.42 ± 0.04	13.94 ± 1.35	43.53 ± 5.4	0.32
Leached	28.98 ± 0.68	2.43 ± 0.23	14.93 ± 0.63	0.66 ± 0.18	49.98 ± 0.74	3.01 ± 0.37	16.60

Considering Figure 4, it is clear that morphological changes occurred during the reduction and acid-leaching procedures of chromite. Table 3 indicates that the Cr/Fe ratio of as-received (Figure 4a) and treated (Figure 4b) chromite particles are 1.77 and 0.32, respectively, suggesting that the surface was enriched with Fe after reduction. The acid-leached chromite particles (Figure 4c) have a Cr/Fe ratio of 16.60. This increase in Cr/Fe ratio suggests that the Fe-enriched surficial layer was removed during the acid-leaching procedure. Hazar-Yoruc (2007) found that cracks, dislocations, and cavities/spaces of the

spinal are ideal locations for the nucleation of Fe [61]. Therefore, the cavities observed on the surface of acid-leached particles (Figure 4c) may be ascribed to the dissolution of Fe. Table 3 further suggests that only Fe was mobile and that Cr likely remained immobile. To gain further insight into the mobility of chromite constituents, treated particles were cross-sectioned and investigated by SEM (Figure 5) and SEM–EDX (Table 4).

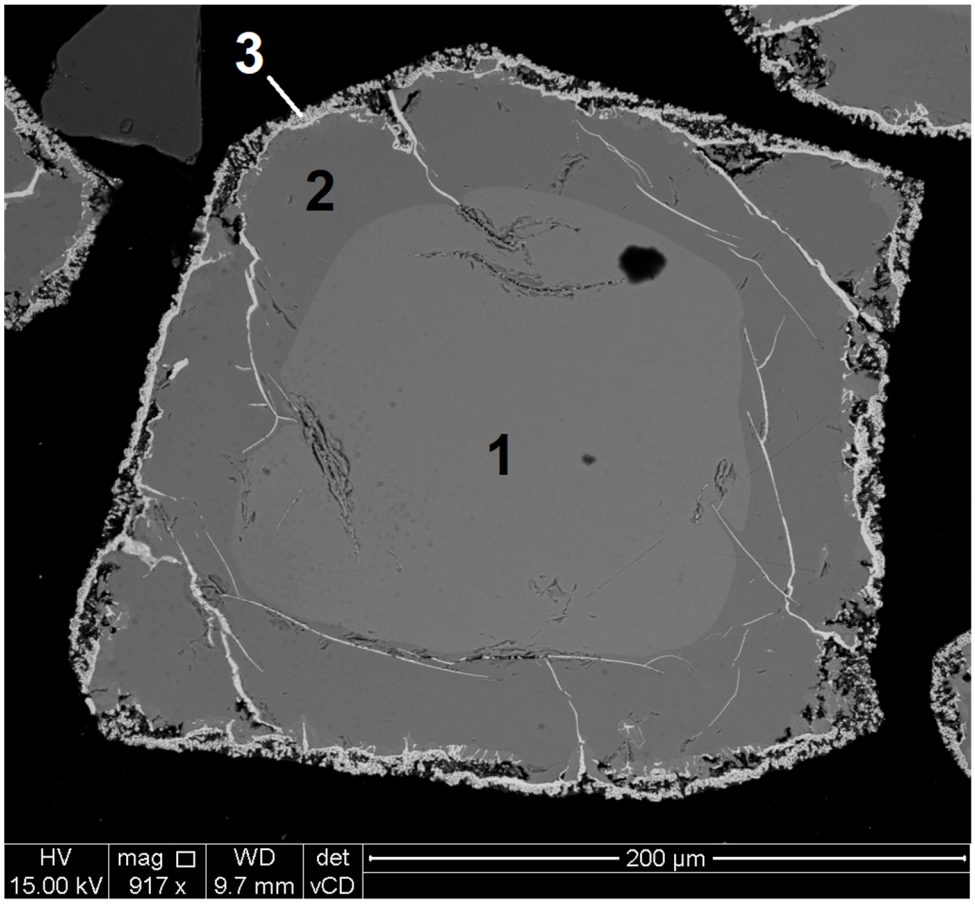

Figure 5. Backscattered electron SEM micrograph of a representative polished cross-sectioned chromite particle thermally treated at 1100 °C for 30 min.

Table 4. SEM–EDX (wt.%) of the center (Area 1), transition phase (Area 2), and rim (Area 3) of a representative particle thermally treated at 1100 °C for 30 min, as well as the respective Cr/Fe, Mg/Fe, and Al/Fe ratio for each of the areas. A minimum of eight randomly selected particles were considered for EDX analysis and between three to five areas were analyzed with the averages and standard deviations indicated.

Cross-Sectioned Particle	Detected Element (wt.%)						Cr/Fe Ratio	Mg/Fe Ratio	Al/Fe Ratio
	O	Mg	Al	Si	Cr	Fe			
Area 1	31.64 ± 0.39	6.19 ± 0.07	8.24 ± 0.04	0.47 ± 0.06	33.41 ± 0.04	20.07 ± 0.31	1.66	0.31	0.41
Area 2	32.42 ± 0.30	8.86 ± 0.08	8.79 ± 0.13	0.38 ± 0.02	40.29 ± 0.10	9.27 ± 0.33	4.35	0.96	0.95
Area 3	3.44 ± 0.13	0.22 ± 0.30	1.53 ± 0.04	0	4.05 ± 0.51	90.38 ± 0.35	0.04	0.002	0.017

Area 1 (center) represents the chromite particle core, Area 2 (transition phase) represents the Fe deprived area, and Area 3 (rim) represents the surficial Fe-enriched layer. The detected O and Cr in Area 3 may be ascribed to the nearby Area 2.

Figure 5 shows that the metalization occurred at the rim (Area 3) of chromite particles. EDX analysis indicates the rim with the composition of 90.4 wt.% Fe and 4.1 wt.% Cr, which

corresponds to a Cr/Fe ratio of 0.04. The O content of 3.4 wt.% indicates that some of the Fe, Cr, Al and Mg concentrations may not be elemental, which may partially be ascribed to the presence of unreduced oxides. However, EDX is a semi-quantitative analytical technique, with O determined by difference. Nevertheless, Area 2 had a relatively low Fe content of 9.3 wt.%, which is ascribed to the migration of Fe towards the particle surface. The Cr/Fe ratio for Area 2 was 4.35, which is significantly higher than the 1.66 Cr/Fe ratio of the particle core (Area 1). A non-related study utilizing the same ore had a similar Cr/Fe ratio (i.e., 1.65) at the particle core [2], which suggests that the total Fe content at the particle center was unaffected.

The migration of Fe (as Fe^{2+} and Fe^{3+}) towards the rim of chromite particles creates vacancies in the octahedral and tetrahedral sites of the chromite spinel [58]. The removal of Fe^{2+} from tetrahedral sites increased the Mg/Fe ratio from 0.31 for Area 1 to 0.96 for Area 2, whereas the removal of Fe^{3+} from octahedral sites increased the Al/Fe ratio from 0.45 for Area 1 to 0.95 for Area 2. Furthermore, the low Mg/Fe and Al/Fe ratios of Area 3 indicate that Mg and Al did not undergo any migration.

As opposed to the significant decrease in Fe observed in Areas 1 and 2 (Table 4), the Cr content remained relatively unchanged. Additionally, the observed increase in the Cr/Fe ratio of 1.66 to 4.35 for Areas 1 and 2 supports the migration of Fe towards the particle rim. This is made evident when considering the Cr/Fe ratio of 0.04 of Area 3.

Soykan et al. (1991) proposed the reduction mechanism of chromite, as well as the subsequent formation of Cr- and Fe-carbides during carbothermic smelting, where carbon is used as the reductant. The reduction mechanism proceeds according to the following four steps [68]: (i) the surface of the chromite particle serves as the location for the chemical reduction reaction where Fe^{2+} is metalized to Fe; (ii) Cr^{2+} ions migrate from the rim to the transition phase (Area 3 to Area 2) via solid-state diffusion; (iii) at the outer edge of the center (Area 1), Fe^{3+} ions are reduced to Fe^{2+} ions, as presented in the following reaction [68]:

$$[Fe^{3+}] + (Cr^{2+}) = (Fe^{2+}) + [Cr^{3+}] \quad \text{(R33)}$$

The round and square brackets refer to the tetrahedral and octahedral sites of the spinel lattice, respectively. The formed Fe^{2+} ions migrate from the center to the rim of the particle via solid-state diffusion. (iv) After the complete reduction of Fe, the remaining Cr^{2+} ions together with the Cr^{3+} ions are reduced to their metallic state (Cr^0), creating Fe- and Cr- depleted spinels of $MgAl_2O_4$ [68].

Though the reaction mechanism proposed by Soykan et al. (1991) is for carbothermic smelting, it is likely true for the employment of hydrogen as a reductant during solid–gas reduction. The use of hydrogen is, however, limited to the reduction mechanism of Fe-oxides as Cr_2O_3 reduction is not evident when considering Tables 3 and 4.

EPMA analysis was employed to determine the chemical compositions of the center (Area 1) and transition phase (Area 2) of treated chromite. The rim (Area 3) was not considered for EPMA as it mainly comprised metallic Fe. The results obtained from EPMA analysis are represented in Table 5.

It is evident from Table 5 that the total Fe content decreased systematically from Untreated to Area 2, and that the total Fe in Area 2 was <1 wt.%. The decrease in total Fe indicates its migration towards the rim (Figure 5), where it occurs as a metallic Fe layer.

The Cr_2O_3 content of Areas 1 and 2 increased from 56.1 to 71.8 wt.%, respectively, which may be ascribed to the migration of Fe^{2+} from Area 2 to Area 3. This observation suggests that Cr remained immobile at the investigated reduction conditions. The migration of Fe towards the rim of the particle further leads to changes in the MgO content within the different grain areas. The presence of MgO in Area 2 is non-appreciable and according to EPMA calculations, Area 2 is dominated by eskolaite with the composition of $Cr_{1.4}Al_{0.6}O_3$. This further suggests that tetrahedral vacancies created in Area 1 were occupied by Mg^{+2} originating from Area 2.

Table 5. EPMA of particle Areas 1 and 2 (as indicated in Figure 4) of ore particles reduced by hydrogen at 1100 °C for 30 min. Table 5 presents 90 spot analyses from Area 1 (center) and 21 spot analyses from Area 2 (transition phase).

Grain Area	Detected Phase (wt,%)						
	TiO_2	Al_2O_3	Cr_2O_3	FeO #	MnO	MgO	NiO
Untreated *	0.97 ± 0.04	11.97 ± 0.18	44.45 ± 0.34	32.14 ± 0.22	0.36 ± 0.02	4.45 ± 0.09	0.12 ± 0.02
Area 1	0.59 ±0.07	16.69 ±0.25	56.14 ±0.75	12.28 ±0.28	0.34 ±0.06	13.71 ±0.17	0.01 ±0.02
Area 2	3.31 ±0.15	21.47 ±0.28	71.82 ±0.86	0.62 ±0.08	0.04 ±0.03	0.67 ±0.04	0.01 ±0.02

* Average values of six microanalyses, data reproduced from Paktunc and Cabri (1995) [72], with permission from Elsevier; # total iron.

Changes in the composition of chromite resulting from reduction by hydrogen are shown in Figure 6 in terms of Mg fraction among the tetrahedral cations and Cr fraction among the octahedral cations in chromite. Increases in the Cr fraction from the original unreacted chromite to Area 1 shown as groups of A and B result from the reduction of Fe^{3+}. With the continued reduction and migration of Fe from the chromite structure, the $Mg/(Mg^{+}Fe^{2+})$ ratio increases from A to B in Figure 6. The highest observed $Mg/(Mg^{+}Fe^{2+})$ ratio is 0.87 indicating the extent of Fe reduction under the experimental conditions.

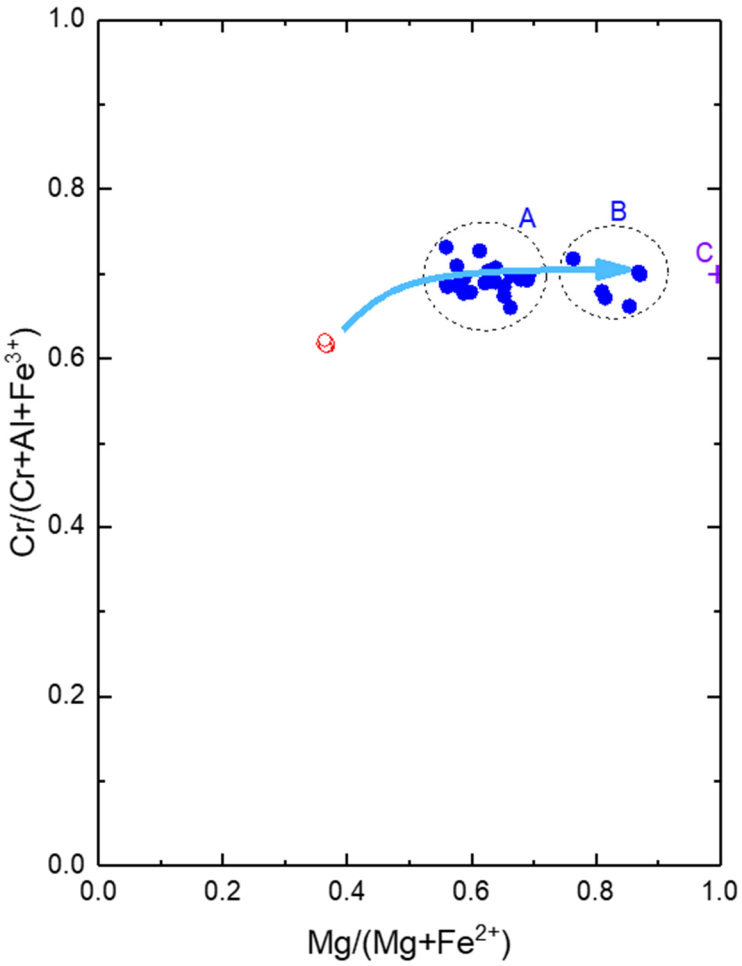

Figure 6. Changes in the composition of chromite resulting from reduction by hydrogen (blue symbols grouped as A and B with average chromite formulas of $Mg_{0.6}Fe_{0.4}Cr_{1.4}Al_{0.6}O_4$ and $Mg_{0.8}Fe_{0.2}Cr_{1.4}Al_{0.6}O_4$, respectively. Original untreated chromite compositions are shown by red circles with an average starting composition of $(Mg_{0.4}Fe_{0.6})(Cr_{1.2}Al_{0.5}Fe_{0.3})O_4$.

According to Figure 6, the removal of Fe from the chromite spinel yields a partially Fe-depleted chromite phase and eskolaite with the composition $Cr_{1.4}Al_{0.6}O_3$ (as determined by EPMA). The extent of reduction is determined by the amount of Fe removed from the chromite spinel. To illustrate this, the following reactions were compiled based on the results presented in Figure 6.

The lowest extent of reduction is indicated as Group A (circled in Figure 6) and is expressed as follows:

$$Mg_{0.4}Fe_{0.6}Cr_{1.2}Al_{0.5}Fe_{0.3}O_4 + 0.75H_2(g) = 0.66\ Mg_{0.6}Fe_{0.4}Cr_{1.4}Al_{0.6}O_4 + 0.2\ Cr_{1.4}Al_{0.6}O_3 + 0.6\ Fe + 0.75\ H_2O\ (g) \quad (R34)$$

Chromite which has undergone a higher extent of reduction than the chromite shown in Reaction (9) is indicated as Group B (circled in Figure 6) and is expressed as follows:

$$Mg_{0.4}Fe_{0.6}Cr_{1.2}Al_{0.5}Fe_{0.3}O_4 + 0.92H_2(g) = 0.5Mg_{0.8}Fe_{0.2}Cr_{1.4}Al_{0.6}O_4 + 0.36Cr_{1.4}Al_{0.6}O_3 + 0.8Fe + 0.92H_2O\ (g) \quad (R35)$$

Chromite which has undergone near-complete removal of Fe from the spinal is indicated with the arrow as part of Group B and is expressed as follows:

$$Mg_{0.4}Fe_{0.6}Cr_{1.2}Al_{0.5}Fe_{0.3}O_4 + 0.97H_2(g) = 0.45Mg_{0.9}Fe_{0.1}Cr_{1.4}Al_{0.6}O_4 + 0.41Cr_{1.4}Al_{0.6}O_3 + 0.85Fe + 0.97H_2O\ (g) \quad (R36)$$

Lastly, chromite which has undergone complete removal of Fe is indicated as C in Figure 6 and is expressed as follows:

$$Mg_{0.4}Fe_{0.6}Cr_{1.2}Al_{0.5}Fe_{0.3}O_4 + H_2(g) = 0.4MgCr_{1.4}Al_{0.6}O_4 + 0.46Cr_{1.4}Al_{0.6}O_3 + 0.9Fe + H_2O\ (g) \quad (R37)$$

Considering Reactions (34)–(37), it is evident that the reduction of the Fe-oxides present in the chromite spinel proceeded systematically and was kinetically limited under parameters considered in this study, i.e., complete removal of Fe was not achieved. Nevertheless, it is theoretically possible to metalize chromite's total Fe-oxide content by selective metalization using hydrogen (Reaction (37)).

3.3. XRD Characterization of Pre-Reduced Chromite Fines

To determine the mineralogical changes occurring within the chromite spinel during reduction, quantitative Rietveld refined XRD analysis was performed on as-received, treated, and leached chromite particles (Figure 7). The treated particles were reduced at 1100 °C for 30 min. The peaks of importance, i.e., eskolaite and metallic Fe, are indicated. The remainder of the unmarked peaks are ascribed to chromite and are not labelled.

Figure 7 shows the formation of metallic Fe and the eskolaite-phase after the thermal treatment of as-received chromite with hydrogen. During the reduction process, Fe is released from the chromite spinel and affords the formation of eskolaite from the spinel structure in the form of exsolution. It was further clear that the applied acid-leaching procedure effectively removed the metalized Fe from the treated chromite, and any remaining Fe may be ascribed to its encapsulation (the confinement of an individual molecule within a larger molecule in the host chromite in the form of fine and minor inclusion).

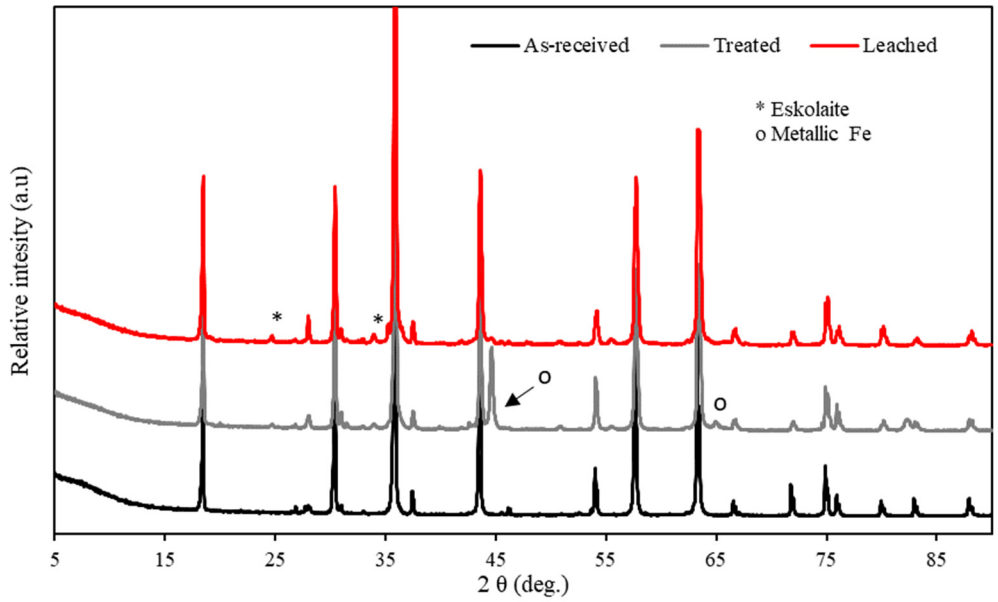

Figure 7. XRD patterns of as-received, treated, and acid-leached chromite.

Considering the formation of the eskolaite phase, it is of importance to determine the effect thereof on the reducibility of hydrogen-treated chromite. An Ellingham diagram was compiled with the HSC thermodynamics program to indicate the change in the reduction ΔG° of pure chromite (Cr_2FeO_4) and eskolaite (shown as Cr_2O_3) by C (Figure 8).

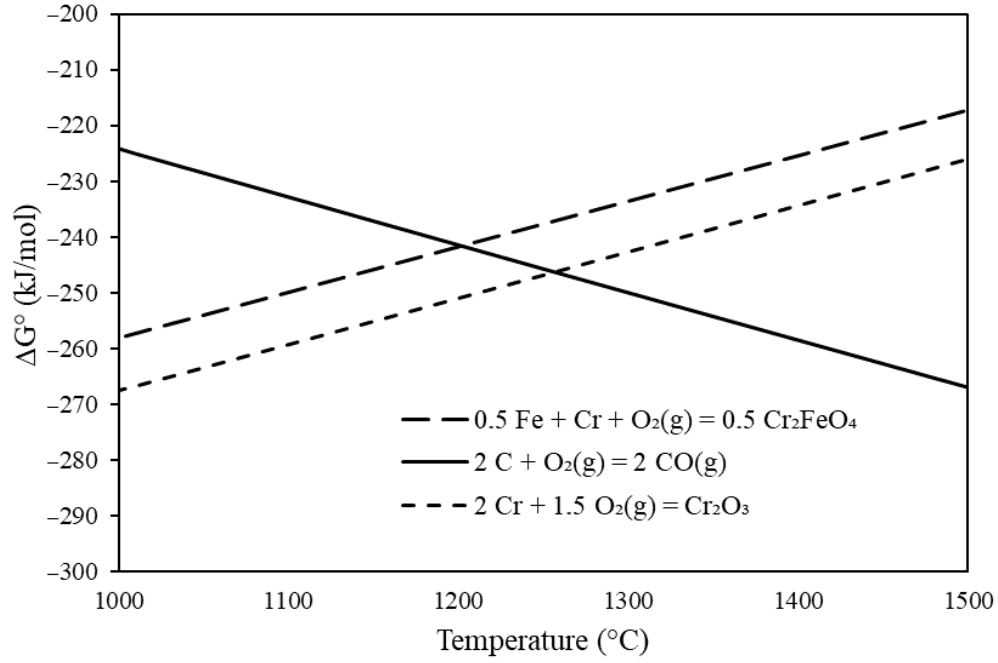

Figure 8. Ellingham diagram (ΔG° as a function of temperature) indicating standard ΔG° of the reduction of Cr_2O_3 and Cr_2FeO_4 with solid C (constructed with HSC thermochemical software) [75].

Figure 8 indicates that synthetic chromite Cr_2FeO_4 is reduced at approximately 1200 °C, whereas Cr_2O_3 reduces at the slightly higher temperature of 1250 °C [13]. The reason is that a sesquioxide solid solution forms between α-Al_2O_3 and Cr_2O_3 that stabilizes eskolaite (i.e., $Cr_{1.4}Al_{0.6}O_3$) against reduction. Both Al_2O_3 and Cr_2O_3 are sesquioxide with a similar corundum crystal structure that could form a range of substitutional corundum-eskolaite-type compounds, e.g., α-$(Al^{3+}, Cr^{3+})_2O_3$, at high temperatures [76]. It is, however,

noted that in practice, the $Cr_{1.4}Al_{0.6}O_3$ phase will have a higher degree of resistance to reduction when compared with Cr_2O_3 due to the stabilizing effect of Al.

According to Kleynhans et al. (2016), the formation of Cr_2O_3 may not necessarily be beneficial, as according to thermodynamical calculations, eskolaite reduces at a slightly higher temperature when compared with pure chromite. Kleyhans et al. (2016) proposed that it is crucial to identify the maximum temperature for Fe-oxide reduction, while minimizing the extent of eskolaite-phase formation [27]. From this study, it is evident that eskolaite-phase formation is ascribed to the removal of Fe from the chromite spinel.

3.4. Effects of Reduction Time and Particle Size on Metalization

To evaluate the effect of particle size on the extent of Fe and Cr metalization, size-partitioned chromite (refer to d_{90} values, Table 1) was reduced at 1100 °C for 30 min (Figure 9). It is evident from Figure 9 that the degree of Fe and Cr metalization increased as the particle size decreased. The smallest size partition (d_{90} of 140 µm) had the highest %Fe and %Cr metalization, i.e., 57% Fe and 7.5% Cr metalization. The lowest percentage metalization was observed for the largest size partition (d_{90} of 941 µm), i.e., 18% Fe and 0.25% Cr metalization.

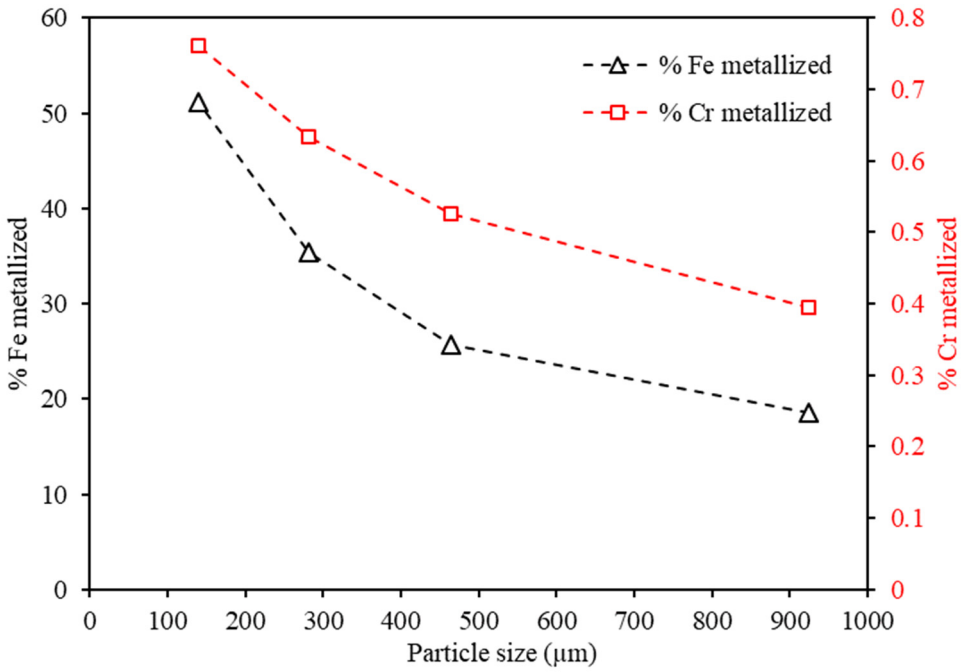

Figure 9. The effect of particle size on Cr and Fe metalization. Thermal treatment was performed at 1100 °C for 30 min.

The observed effect of particle size on chromite metalization was, however, expected, considering that the larger particle surface area is present for the smallest size partition (d_{90} of 140 µm), affording a greater chromite/hydrogen contact boundary when compared with the largest size partition (d_{90} of 941 µm). Moreover, during the initial phase of the reduction reaction, the reaction occurs at the surface and sub-surface of the chromite particles, which suggests a relatively short diffusion path for both Fe-movement and hydrogen penetration [61,68].

To evaluate the effect of reduction time on the extent of Cr and Fe metalization, the size-partitioned chromite was reduced isothermally at 1100 °C for between 0 and 30 min (Figure 10).

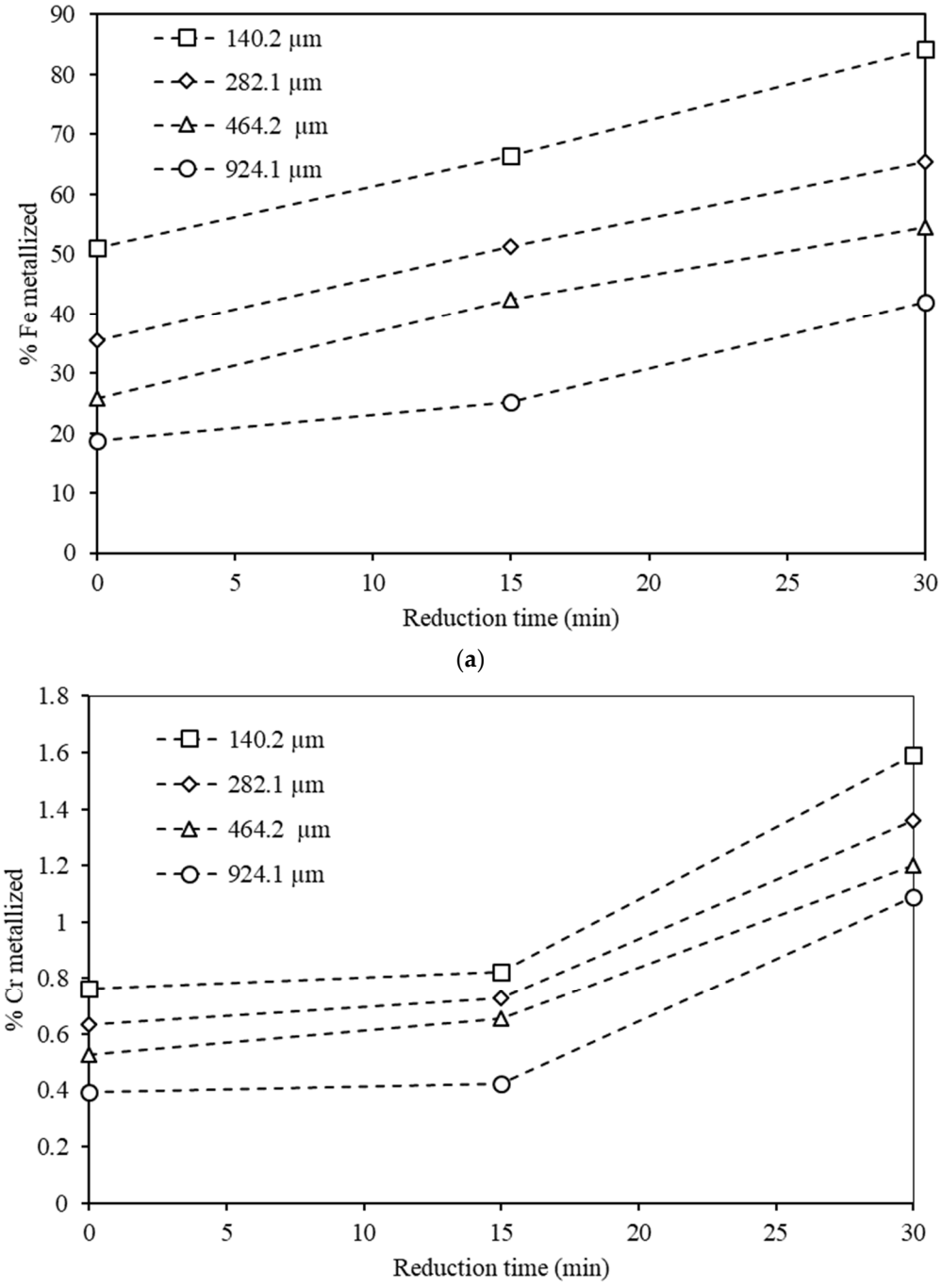

Figure 10. The effects of reduction time on (**a**) Fe and (**b**) Cr metalization during isothermal treatment at 1100 °C.

Figure 10a further shows that the %Fe reduction had a near-linear trend. The %Fe metalization increased systematically from 51 to 84% for the smallest size fraction (d_{90} of 140.2 µm) as the isothermal reduction time increased from 0 to 30 min. A similar trend was observed for all other size fractions (d_{90} of 282.1 to 924.1 µm). Considering the relatively linear %Fe, it is likely that the formation of the surficial Fe layer did not curtail hydrogen's accessibility to the underlying Fe-oxides present in the bulk material.

For all four particle sizes fractions, Figure 10b indicates very little Cr metalization during the first fifteen minutes of the reduction process, followed by a relatively significant increase in metalization. This can likely be explained by the ionic diffusion mechanism

proposed by Soykan et al. that suggests reduced Cr^{2+} is metalized to Cr^{0} after the complete reduction of Fe [68]. However, considering that the highest %Cr metalization did not exceed 1.52%, it is evident that the reduction of Cr-oxide present in the chromite spinel was insignificant under the investigated conditions.

It can, therefore, be concluded that the metalization of Fe-oxides present in chromite occurs readily, whereas Cr-oxide metalization was insignificant.

3.5. Practical Implementation

This study was mainly dedicated to exploring the fundamentals of incorporating hydrogen as a reductant during chromite smelting. To guide further development, it is worth mentioning the limitations of the current study and aspects that need to be considered in the future. It is further important to consider the existing infrastructure of FeCr smelters, and the chemical properties of hydrogen, when developing an approach to incorporate hydrogen as a reductant.

Firstly, existing industrial processes employing high temperatures before smelting are considered. A significant fraction of chromite is beneficiated and pelletized via two high-temperature processes [28]. The existing pellet curing processes are summarized thus: (i) oxidative sintered pellets are generated by batching chromite, 1 to 2 wt.% carbonaceous reductant fines such as (coke, gas coke, char, and anthracite), and 1 wt.% refined clay (usually bentonite). Green pellets are then generated in a pelletization drum and cured/sintered between 1400 to 1500 °C [6,77]; and (ii) pre-reduced pellets are generated by batching chromite ore, 12 to 14 wt.% carbonaceous reductant, and 3 to 4.5 wt.% clay binder [6]. The green pellets are then cured/pre-reduced between 1300 to 1400 °C [3,6]. The hot pre-reduced green pellets are fed directly without being screened to a closed SAFs [78,79].

In both pellet-curing processes, green pellets are directly exposed to thermal energy sources. The incorporation of hydrogen directly into the pellet-curing kilns as part of the kiln atmosphere is perplexed by the combustion properties hydrogen. For instance, hydrogen has a flammability range (in air) of 4–75 vol.%, an auto-ignition temperature of approximately 570 °C, and minimum ignition energy of 0.02 mJ [57,59,80–82]. Therefore, hydrogen ignition would be a certainty within its combustion range, if the required amount of oxygen is present within the furnace atmosphere. Nevertheless, the addition of hydrogen outside its 4–75 vol.% flammability range is possible but would be a major safety concern and operational perplexity.

Considering the latter, the incorporation of hydrogen as a reductant will require a designated process as its incorporation into existing infrastructure is unlikely. Selecting a suitable furnace is critical, and the employment of an enclosed and externally heated furnace is the evident choice. Nevertheless, internal heating using hot gas could also be considered.

The stage at which the hydrogen treatment is incorporated in the overall chromite smelting process is another critical consideration. Two scenarios are considered here: (i) run-off-mine ore (ore as recovered from mines) is treated before beneficiation and an Fe-separation step (magnetic, chemical, or density) is included as part of the beneficiation circuit; and (ii) cured pelletized chromite is subjected to hydrogen treatment. Considering the two pellet types (oxidative sintered and pre-reduced), the effects of hydrogen treatment on oxidized and pre-reduced chromite should be determined. It is, however, likely that the hydrogen treatment of pre-reduced pellets would not be beneficial, as a significant fraction of Fe would already be in a metallic state [83].

Considering this section, it is clear that further research is required on the use of hydrogen and its real-world application. It is proposed that further fundamental research be conducted to quantify kinetic parameters for the different reactions as a basis for process design. Hereafter, a comprehensive techno-economic study be performed.

4. Conclusions

In this paper, we present the reduction of naturally occurring chromite using hydrogen. It was shown that the reduction of $Fe^{3+} \rightarrow Fe^{2+}$ and $Fe^{2+} \rightarrow Fe^{0}$ for as-received chromite, initiates at 500 and 846 °C, respectively. It was found that three distinct areas were present within chromite particles after hydrogen reduction, i.e., a rim area enriched by metallic Fe, an Fe-deprived transition phase, and a center phase representative of untreated chromite. The Cr/Fe ratios of the rim, transition phase, and center were 0.04, 4.35, and 1.66, respectively.

Removal of the Fe layer by hot-acid leaching revealed an underlying eskolaite-phase ($Cr_{1.4}Al_{0.6}O_3$), which suggests the exsolution of at least a fraction of chromite's Cr-oxide content. Preliminary tests showed that particle size had a relatively significant effect on the % Fe and Cr metalization. Also, the % Fe metalization increased near-linearly with increasing reduction time, while the % Cr metalization showed a relatively appreciable increase as the % Fe metalization increased. The highest % Fe metalization was achieved for chromite with a d_{90} value of 140.2 µm, treated with hydrogen at 1100 °C for 30 min, while the % Cr metalized was approximately 1.52%. This suggests that, under the considered experimental parameters, the Cr-oxide content of chromite was essentially unaffected.

Lastly, we indicate the limitations of employing hydrogen as a chromite reductant and indicate that its incorporation into existing infrastructure is unlikely. Specialized alterations to existing infrastructure are required to prevent unwanted hydrogen ignition during operations. We further propose that significant research and development is required before hydrogen can be employed as a real-world chromite reductant.

Author Contributions: Conceptualization, S.P.D.P. and J.D.; methodology, S.P.D.P., J.D. and J.P.B.; software, J.D. and J.J.R.-H.; validation, S.P.D.P., D.P., M.T. and E.R.; formal analysis, J.D.; investigation, J.D., S.P.D.P., D.P., J.J.R.-H.; resources, S.P.D.P., D.G.B.; data curation, J.D.; writing—original draft preparation, J.D.; writing—review and editing, J.D., D.P., M.T., E.R., S.P.D.P.; visualization, J.D., J.J.R.-H.; supervision, S.P.D.P.; project administration, S.P.D.P. and M.T.; funding acquisition, M.T. and D.G.B. All authors have read and agreed to the published version of the manuscript.

Funding: This study and APC was funded by the Research Council of Norway (RCN) as the Thanos project (INPART Project 309475) and is acknowledged. The Department of Science and Innovation, South Africa, and HySA Infrastructure Centre of Competence, South Africa, are also acknowledged for financial support through the KP5 program.

Data Availability Statement: Not applicable.

Acknowledgments: The authors thank Nico Lemmer, Kosie Oosthuizen, Sarel Naude, and Thabo Diobe at the North-West University for assistance provided during sample preparation and analysis. Thanks are also given to Derek Smith and Dominique Duguay at CANMET for XRD and electron microprobe analyses, respectively.

Conflicts of Interest: The authors declare no conflict of interest.

References

1. Tathavadkar, V.D.; Antony, M.; Jha, A. The physical chemistry of thermal decomposition of South African chromite minerals. *Metall. Mater. Trans. B* **2005**, *36*, 75–84. [CrossRef]
2. Du Preez, S.P.; Beukes, J.P.; Paktunc, D.; Van Zyl, P.G.; Jordaan, A. Recycling pre-oxidized chromite fines in the oxidative sintered pellet production process. *J. S. Afr. Inst. Min. Metall.* **2019**, *119*, 207–215. [CrossRef]
3. Riekkola-Vanhanen, M. Finnish expert report on best available techniques in ferrochromium production. *Environ. Sci.* **1999**, *314*, 1–49.
4. Du Preez, S.; Beukes, J.; Van Dalen, W.; Van Zyl, P.; Paktunc, D.; Loock-Hattingh, M. Aqueous solubility of Cr (VI) compounds in ferrochrome bag filter dust and the implications thereof. *Water SA* **2017**, *43*, 298–309. [CrossRef]
5. Du Preez, S.; Beukes, J.; Van Zyl, P.; Tangstad, M.; Tiedt, L. Silicon carbide formation enhanced by in-situ-formed silicon nitride: An approach to capture thermal energy of co-rich off-gas combustion. *Metall. Mater. Trans. B* **2018**, *49*, 3151–3163. [CrossRef]
6. Basson, J.; Daavittila, J. High Carbon Ferrochrome Technology. In *Handbook of Ferroalloys*; Elsevier: Amsterdam, The Netherlands, 2013; pp. 317–363.

7. Murthy, Y.R.; Tripathy, S.K.; Kumar, C.R. Chrome ore beneficiation challenges & opportunities–A review. *Miner. Eng.* **2011**, *24*, 375–380.
8. Beukes, J.P.; Dawson, N.F.; Van Zyl, P.G. Theoretical and practical aspects of Cr (VI) in the South African ferrochrome industry. *J. S. Afr. Inst. Min. Metall.* **2010**, *110*, 743–750.
9. Neizel, B.W.; Beukes, J.P.; van Zyl, P.G.; Dawson, N.F. Why is $CaCO_3$ not used as an additive in the pelletised chromite pre-reduction process? *Miner. Eng.* **2013**, *45*, 115–120. [CrossRef]
10. Ringdalen, E.; Rocha, M.; Figueiredo, P. Energy consumption during HCFeCr production at Ferbasa. *INFACON* **2015**, *2*, 668–675. Available online: http://repositoriosenaiba.fieb.org.br/handle/fieb/702 (accessed on 12 January 2022).
11. Ringdalen, E.; Rocha, M.; Figueiredo, P.; Tangstad, M. Pretreatment of Jaccurici Ore from Ferbasa-Brazil: Effect on Energy Consumption. In *2015-Sustainable Industrial Processing Summit*; Flogen Star OUTREACH: Quebec, QC, Canada, 2015; pp. 83–92.
12. Barnes, A.; Finn, C.; Algie, S. The prereduction and smelting of chromite concentrate of low chromium-to-iron ratio. *J. S. Afr. Inst. Min. Metall.* **1983**, *83*, 49–54.
13. Niemelä, P.; Krogerus, H.; Oikarinen, P. Formation, Characteristics and Utilisation of CO-Gas Formed in Ferrochromium Smelting. In *Tenth International Ferro Alloys Congress*; INFACON XI: Cape Town, South Africa, 2004; pp. 68–77.
14. Du Preez, S.P. *Cr (VI) Generation during Flaring of Off-Gas from Closed Ferrochromium Submerged Arc Furnaces*; North-West University, Potchefstroom Campus: Potchefstroom, South Africa, 2014.
15. Du Preez, S.; Beukes, J.; Van Zyl, P. Cr (VI) generation during flaring of CO-rich off-gas from closed ferrochromium submerged arc furnaces. *Metall. Mater. Trans. B* **2015**, *46*, 1002–1010. [CrossRef]
16. Beukes, J.; Du Preez, S.; Van Zyl, P.; Paktunc, D.; Fabritius, T.; Päätalo, M.; Cramer, M. Review of Cr (VI) environmental practices in the chromite mining and smelting industry–Relevance to development of the Ring of Fire, Canada. *J. Clean. Prod.* **2017**, *165*, 874–889. [CrossRef]
17. Winter, F. Production of Chromium Iron Alloys Directly from Chromite Ore. WO2015060951A1, 30 April 2016.
18. Pheiffer, D.M.; Cookson, K. Ferrochrome Alloy Production. WO2015159268A1, 22 October 2015.
19. Yu, D.; Paktunc, D. Calcium chloride-assisted segregation reduction of chromite: Influence of reductant type and the mechanism. *Minerals* **2018**, *8*, 45. [CrossRef]
20. Yu, D.; Paktunc, D. Carbothermic Direct Reduction of Chromite Using a Catalyst for the Production of Ferrochrome Alloy. WO2018201218A1, 8 November 2021.
21. Yu, D.; Paktunc, D. Direct production of ferrochrome by segregation reduction of chromite in the presence of calcium chloride. *Metals* **2018**, *8*, 69. [CrossRef]
22. Sokhanvaran, S.; Paktunc, D. Method of Direct Reduction of Chromite with Cryolite Additive. U.S. Patent 20190119784A1, 25 April 2019.
23. Canaguier, V. Synthesis and Reduction-Carburization of (Fe, Mg)(Cr, Al)$_2O_4$ Composite Spinel Solid Solution with CH4. Ph.D. Thesis, Norwegian University of Science and Technology, Trondheim, Norway, 2018.
24. Anacleto, N.; Ostrovski, O. Solid-state reduction of chromium oxide by methane-containing gas. *Metall. Mater. Trans. B* **2004**, *35*, 609–615. [CrossRef]
25. Suzuki, A.; Yasuda, A.; Ozawa, K. Cr and Al diffusion in chromite spinel: Experimental determination and its implication for diffusion creep. *Phys. Chem. Miner.* **2008**, *35*, 433–445. [CrossRef]
26. ICDA. Statistical Bulletin 2013. Available online: https://www.icdacr.com/download/ICDAActivityReport2013.pdf (accessed on 25 September 2021).
27. Kleynhans, E.; Neizel, B.; Beukes, J.; Van Zyl, P. Utilisation of pre-oxidised ore in the pelletised chromite pre-reduction process. *Miner. Eng.* **2016**, *92*, 114–124. [CrossRef]
28. Glastonbury, R.I.; Beukes, J.; Van Zyl, P.; Sadikit, L.; Jordaan, A.; Campbell, Q.; Stewart, H.; Dawson, N. Comparison of physical properties of oxidative sintered pellets produced with UG2 or metallurgical-grade South African chromite: A case study. *J. S. Afr. Inst. Min. Metall.* **2015**, *115*, 699–706. [CrossRef]
29. Ringdalen, E.; Olsen, S.E. The effect of chromite ore mineralogy on reduction mechanisms and reducibility. *INFACON* **1998**, *8*, 147–152.
30. Pandey, B.; Prajapati, Y.K.; Sheth, P.N. Recent progress in thermochemical techniques to produce hydrogen gas from biomass: A state of the art review. *Int. J. Hydrogen Energy* **2019**, *44*, 25384–25415. [CrossRef]
31. Canavesio, C.; Nassini, D.; Nassini, H.E.; Bohé, A.E. Study on an original cobalt-chlorine thermochemical cycle for nuclear hydrogen production. *Int. J. Hydrogen Energy* **2019**, *45*, 26090–26103. [CrossRef]
32. Falch, A.; Kriek, R.J. Laser induced H_2 production employing Pt-TiO_2 photocatalysts. *J. Photochem. Photobiol. A Chem.* **2013**, *271*, 117–123. [CrossRef]
33. Zhang, J.; Xing, C.; Shi, F. MoS_2/Ti_3C_2 heterostructure for efficient visible-light photocatalytic hydrogen generation. *Int. J. Hydrogen Energy* **2020**, *45*, 6291–6301. [CrossRef]
34. Ziming, C.; Fuqiang, W.; Huaxu, L.; Shengpeng, H.; Bo, L.; Jianyu, T.; Hongyang, L. Photon-absorption-based explanation of ultrasonic-assisted solar photochemical splitting of water to improve hydrogen production. *Int. J. Hydrogen Energy* **2018**, *43*, 14439–14450. [CrossRef]
35. Liu, W.-S.; Perng, T.-P. Ta_2O_5 hollow fiber composed of internal interconnected mesoporous nanotubes and its enhanced photochemical H2 evolution. *Int. J. Hydrogen Energy* **2019**, *44*, 17688–17696. [CrossRef]

36. Patel, P.P.; Ghadge, S.D.; Hanumantha, P.J.; Datta, M.K.; Gattu, B.; Shanthi, P.M.; Kumta, P.N. Active and robust novel bilayer photoanode architectures for hydrogen generation via direct non-electric bias induced photo-electrochemical water splitting. *Int. J. Hydrogen Energy* **2018**, *43*, 13158–13176. [CrossRef]
37. Manwar, N.R.; Borkar, R.G.; Khobragade, R.; Rayalu, S.S.; Jain, S.L.; Bansiwal, A.K.; Labhsetwar, N.K. Efficient solar photo-electrochemical hydrogen generation using nanocrystalline $CeFeO_3$ synthesized by a modified microwave assisted method. *Int. J. Hydrogen Energy* **2017**, *42*, 10931–10942. [CrossRef]
38. Du Preez, S.P.; Bessarabov, D.G. Hydrogen generation by means of hydrolysis using activated Al-In-Bi-Sn composites for electrochemical energy applications. *Int. J. Electrochem. Sci.* **2017**, *12*, 8663–8682. [CrossRef]
39. Du Preez, S.P.; Bessarabov, D.G. Hydrogen generation of mechanochemically activated Al-Bi-In composites. *Int. J. Hydrogen Energy* **2017**, *42*, 16589–16602. [CrossRef]
40. Du Preez, S.P.; Bessarabov, D.G. Hydrogen generation by the hydrolysis of mechanochemically activated aluminum-tin-indium composites in pure water. *Int. J. Hydrogen Energy* **2018**, *43*, 21398–21413. [CrossRef]
41. Du Preez, S.P.; Bessarabov, D.G. The effects of bismuth and tin on the mechanochemical processing of aluminum-based composites for hydrogen generation purposes. *Int. J. Hydrogen Energy* **2019**, *44*, 21896–21912. [CrossRef]
42. Du Preez, S.P.; Bessarabov, D.G. Material Aspects Pertaining to Hydrogen Production from Aluminum: Opinion. *Res. Dev. Mater. Sci.* **2019**, *44*, 21896–21912. [CrossRef]
43. Du Preez, S.P. *Hydrogen Generation by the Reaction of Mechanochemically Activated Aluminium and Water*; North-West University: Potchefstroom, South Africa, 2019.
44. du Preez, S.P.; Bessarabov, D.G. On-demand hydrogen generation by the hydrolysis of ball-milled aluminum composites: A process overview. *Int. J. Hydrogen Energy* **2021**, *46*, 35790–35813. [CrossRef]
45. Bessarabov, D.G.; Human, G.; Kruger, A.J.; Chiuta, S.; Modisha, P.M.; du Preez, S.P.; Oelofse, S.P.; Vincent, I.; Van Der Merwe, J.; Langmi, H.W.; et al. South African hydrogen infrastructure (HySA infrastructure) for fuel cells and energy storage: Overview of a projects portfolio. *Int. J. Hydrogen Energy* **2017**, *42*, 13568–13588. [CrossRef]
46. Phillips, R.; Dunnill, C.W. Zero gap alkaline electrolysis cell design for renewable energy storage as hydrogen gas. *RSC Adv.* **2016**, *6*, 100643–100651. [CrossRef]
47. Falch, A.; Badets, V.A.; Labrugère, C.; Kriek, R.J. Co-sputtered PtxPdyAlz thin film electrocatalysts for the production of hydrogen via SO_2 (aq) electro-oxidation. *Electrocatalysis* **2016**, *7*, 376–390. [CrossRef]
48. Vincent, I.; Bessarabov, D. Low cost hydrogen production by anion exchange membrane electrolysis: A review. *Renew. Sustain. Energy Rev.* **2018**, *81*, 1690–1704. [CrossRef]
49. Vincent, I.; Kruger, A.; Bessarabov, D. Development of efficient membrane electrode assembly for low cost hydrogen production by anion exchange membrane electrolysis. *Int. J. Hydrogen Energy* **2017**, *42*, 10752–10761. [CrossRef]
50. Merwe, J.V.D.; Uren, K.; Schoor, G.V.; Bessarabov, D. A study of the loss characteristics of a single cell PEM electrolyser for pure hydrogen production. In Proceedings of the 2013 IEEE International Conference on Industrial Technology (ICIT), Cape Town, South Africa, 25–28 February 2013; pp. 668–672.
51. Chiuta, S.; Everson, R.C.; Neomagus, H.W.J.P.; Bessarabov, D.G. Hydrogen production from ammonia decomposition over a commercial Ru/Al_2O_3 catalyst in a microchannel reactor: Experimental validation and CFD simulation. *Int. J. Hydrogen Energy* **2016**, *41*, 3774–3785. [CrossRef]
52. Chiuta, S.; Everson, R.C.; Neomagus, H.W.J.P.; Bessarabov, D.G. Performance evaluation of a high-throughput microchannel reactor for ammonia decomposition over a commercial Ru-based catalyst. *Int. J. Hydrogen Energy* **2015**, *40*, 2921–2926. [CrossRef]
53. Chiuta, S.; Everson, R.C.; Neomagus, H.W.J.P.; van der Gryp, P.; Bessarabov, D.G. Reactor technology options for distributed hydrogen generation via ammonia decomposition: A review. *Int. J. Hydrogen Energy* **2013**, *38*, 14968–14991. [CrossRef]
54. Sekoai, P.T.; Ouma, C.N.M.; du Preez, S.P.; Modisha, P.; Engelbrecht, N.; Bessarabov, D.G.; Ghimire, A. Application of nanoparticles in biofuels: An overview. *Fuel* **2019**, *237*, 380–397. [CrossRef]
55. Sekoai, P.T.; Engelbrecht, N.; du Preez, S.P.; Bessarabov, D. Thermophilic Biogas Upgrading via ex Situ Addition of H_2 and CO_2 Using Codigested Feedstocks of Cow Manure and the Organic Fraction of Solid Municipal Waste. *ACS Omega* **2020**, *5*, 17367–17376. [CrossRef]
56. Sekoai, P.T.; Daramola, M.O.; Mogwase, B.; Engelbrecht, N.; Yoro, K.O.; du Preez, S.P.; Mhlongo, S.; Ezeokoli, O.T.; Ghimire, A.; Ayeni, A.O.; et al. Revising the dark fermentative H_2 research and development scenario—An overview of the recent advances and emerging technological approaches. *Biomass Bioenergy* **2020**, *140*, 105673. [CrossRef]
57. Du Toit, M.H.; Avdeenkov, A.V.; Bessarabov, D. Reviewing H_2 combustion: A case study for non-fuel-cell power systems and safety in passive autocatalytic recombiners. *Energy Fuels* **2018**, *32*, 6401–6422. [CrossRef]
58. Gervilla, F.; Asta, M.P.; Fanlo, I.; Grolimund, D.; Ferreira-Sánchez, D.; Samson, V.A.; Hunziker, D.; Colas, V.; González-Jiménez, J.M.; Kerestedjian, T.N.; et al. Diffusion pathways of Fe2+ and Fe3+ during the formation of ferrian chromite: A μXANES study. *Contrib. Mineral. Petrol* **2019**, *17*, 65. [CrossRef]
59. Du Preez, S.; Jones, D.; Warwick, M.; Falch, A.; Sekoai, P.; das Neves Quaresma, C.M.; Bessarabov, D.; Dunnill, C. Thermally stable Pt/Ti mesh catalyst for catalytic hydrogen combustion. *Int. J. Hydrogen Energy* **2020**, *45*, 16851–16864. [CrossRef]
60. Algie, S.H.; Finn, C.W.P. *Reaction Mechanisms in the Reduction of Winterveld Chrome Spinel with Graphite and Carbon*; Council for Mineral Technology: Randburg, South Africa, 1984.
61. Hazar-Yoruc, A. Reduction mechanism of chromite spinel with carbon. *Min. Metall. Explor.* **2007**, *24*, 115–120. [CrossRef]

62. Ramos-Hernandez, J.J.; Porcayo-Calderon, J.; Salinas-Bravo, V.M.; Arrieta-Gonzalez, C.D.; Gonzalez-Rodriguez, J.G.; Martinez-Gomez, L. Phase Stability Diagrams for High Temperature Corrosion Processes. *Math. Probl. Eng.* **2013**, *2013*, 542061. [CrossRef]
63. Burcat, A.; Ruscic, B. *Third Millenium Ideal Gas and Condensed Phase Thermochemical Database for Combustion (with Update from Active Thermochemical Tables)*; Argonne National Laboratory(ANL): Argonne, IL, USA, 2005.
64. Beverskog, B.; Puigdomenech, I. Revised pourbaix diagrams for chromium at 25–300 °C. *Corros. Sci.* **1997**, *39*, 43–57. [CrossRef]
65. Khan, H.R.; Raub, C.J. Properties of chromium hydride. *J. Less Common Met.* **1976**, *49*, 399–406. [CrossRef]
66. Venkatraman, M.; Neumann, J.P. The cr-h (chromium-hydrogen) system. *J. Phase Equilibria* **1991**, *12*, 672–677. [CrossRef]
67. Dellien, I.; Hall, F.; Hepler, L.G. Chromium, molybdenum, and tungsten: Thermodynamic properties, chemical equilibriums, and standard potentials. *Chem. Rev.* **1976**, *76*, 283–310. [CrossRef]
68. Soykan, O.; Eric, R.; King, R. Kinetics of the reduction of Bushveld complex chromite ore at 1416 C. *Metall. Mater. Trans. B* **1991**, *22*, 801–810. [CrossRef]
69. Xiao, Y.; Yang, Y.; Holappa, L.; Boom, R. Microstructure changes of chromite reduced with CO gas. *INFACON XI New Delhi* **2007**, *1*, 7–14.
70. Słowiński, G.; Smoliński, A. Thermodynamic Feasibility of Hydrogen-Rich Gas Production Supported by Iron Based Chemical Looping Process. *J. Chem.* **2016**, *2016*, 1764670. [CrossRef]
71. Chu, W.F.; Rahmel, A. The kinetics of the reduction of chromium oxide by hydrogen. *Metall. Trans. B* **1979**, *10*, 401–407. [CrossRef]
72. Paktunc, A.; Cabri, L. A proton-and electron-microprobe study of gallium, nickel and zinc distribution in chromian spinel. *Lithos* **1995**, *35*, 261–282. [CrossRef]
73. Zhang, B.; Shi, P.; Jiang, M. Advances towards a clean hydrometallurgical process for chromite. *Minerals* **2016**, *6*, 7. [CrossRef]
74. Xiao, Y.; Schuffeneger, C.; Reuter, M.; Holappa, L.; Seppala, T. *Solid State Reduction of Chromite with CO*; INFACON XI: Cape Town, South Africa, 2004; pp. 26–35.
75. Roine, A.; Lamberg, P.; Katiranta, T.; Salminen, J. *HSC Chemistry 7 Simulation*; Outotec Research: Pori, Finland, 2009.
76. Bondioli, F.; Ferrari, A.M.; Leonelli, C.; Manfredini, T.; Linati, L.; Mustarelli, P. Reaction Mechanism in Alumina/Chromia (Al_2O_3–Cr_2O_3) Solid Solutions Obtained by Coprecipitation. *J. Am. Ceram. Soc.* **2000**, *83*, 2036–2040. [CrossRef]
77. Visser, M. An overview of the history and current operational facilities of Samancor Chrome. *S. Afr. Pyrometall.* **2006**, *2006*, 285–296.
78. Naiker, O. The development and advantages of Xstrata's Premus Process. In *XI International Ferroalloys Congress*; INFACON XI: New Delhi, India, 2006; pp. 113–119.
79. Du Preez, S.P. Ferrochrome Waste Management: Addressing Current Gaps. Ph.D. Thesis, North-West University, Potchefstroom, South Africa, 2018.
80. Kozhukhova, A.E.; du Preez, S.P.; Malakhov, A.A.; Bessarabov, D.G. A Thermally Conductive Pt/AAO Catalyst for Hydrogen Passive Autocatalytic Recombination. *Catalysts* **2021**, *11*, 491. [CrossRef]
81. Malakhov, A.; du Toit, M.H.; Du Preez, S.P.; Avdeenkov, A.; Bessarabov, D. Temperature profile mapping over a catalytic unit of a hydrogen passive autocatalytic recombiner: An experimental and computational fluid dynamics study. *Energy Fuels* **2020**, *34*, 11637–11649. [CrossRef]
82. Du Preez, S.; Jones, D.; Bessarabov, D.; Falch, A.; das Neves Quaresma, C.M.; Dunnill, C. Development of a Pt/stainless steel mesh catalyst and its application in catalytic hydrogen combustion. *Int. J. Hydrogen Energy* **2019**, *44*, 27094–27106. [CrossRef]
83. Kleynhans, E.L.J.; Beukes, J.P.; Van Zyl, P.G.; Bunt, J.R.; Nkosi, N.S.B.; Venter, M. The Effect of Carbonaceous Reductant Selection on Chromite Pre-reduction. *Metall. Mater. Trans. B* **2017**, *48*, 827–840. [CrossRef]